CHAPTER ONE
INTRODUCTION

1.1 PROBLEM STATEMENT

Anthropogenic changes to natural land cover are being driven by a need to provide water, food and shelter to more than six billion people [1]. Unfortunately, these changes have a major impact on hydrology, biodiversity, climate, socio-economic stability and food security [1, 2]. Changes in land-use contribute to human impact on the climate as we are changing the natural rate of exchange of carbon dioxide between the atmosphere and the terrestrial biosphere, for example huge stocks of carbon are released as a result of deforestation [2, 3].

The most pervasive form of land-cover change in South Africa is human settlement expansion [4]. In many cases, new human settlements and settlement expansion are informal and occur in areas that were previously covered by natural vegetation. Informal or unplanned settlements usually evolve as people move closer to employment opportunities [4]. These settlements can occur in various locations and are normally without basic services, which includes electricity, running-water, water-borne sewage and refuse removal. The spatial layout is often not planned but informally developed by the inhabitants of the settlements themselves [5]. Figure 1.1 shows an informal settlement in the Limpopo province of South Africa which developed between 2003 and 2009 in an area that was initially mostly covered by natural vegetation.

A report from the nineteenth special session of the general assembly of the United Nations (UN) identified sustainable human settlements as a matter requiring urgent attention and states that local government needs to be empowered to plan, implement, develop and manage human settlements [6]. It further states that local government needs to be enabled to manage existing informal settlements, and prevent the establishment of new ones. The occurrence of new small rural villages and scattered

FIGURE 1.1: QuickBird image of a new settlement development (courtesy of Google^{TM}Earth)

settlements is difficult to monitor by local government as the majority are informal and erected rapidly without the prior consent of the relevant government or municipal authorities. This leads to inadequate water, water-borne sewage and refuse removal provision [7]. Settlements are infrequently mapped on an ad-hoc basis in South Africa. It follows that determining where and when new informal settlements occur is beneficial not only from an environmental, but also from a socio-economic point of view.

1.2 OBJECTIVE OF THIS THESIS

As shown in the previous section, there exists a need to perform regular land cover change evaluations to identify change areas of interest. Change detection can be defined as the process of identifying differences in the state of an area by observing it at different times [8]. Human operator-dependent change mapping through visual interpretation of imagery is time consuming and resource intensive. Hence there is a need for automated change detection to reduce operator dependence and to enable large datasets to be processed frequently [9, 10].

Remote sensing is the science of obtaining information on an object or area without being in contact with the object or area under investigation [11]. Using various sensors, data are acquired remotely and analyzed to obtain information on the area that is measured by the sensor. Coarse resolution remotely sensed data provides an effective mechanism to monitor large areas on a frequent basis as the wide swath (2000 – 3000 km) of coarse resolution sensors (250 – 1000 m pixel size) enables the same area to be observed at a very high temporal sampling rate (near daily), thus resulting in a highly sampled (hyper-temporal) coarse spatial resolution time-series. This hyper-temporal time-series could

potentially be used as a first step as a change alarm leading to further investigation using higher resolution sensors such as Landsat 7, Ikonos, and QuickBird [12].

Automated land-cover change detection at regional or global scales, using hyper-temporal, coarse resolution satellite data has been a highly desired [13], but elusive goal of environmental remote sensing and has even been described by some as the “holy grail” of remote sensing [9].

Digital change detection encompasses the quantification of temporal phenomena from multi-date imagery that is usually acquired by satellite-based, multi-spectral sensors [14, 15]. Land-cover change can be categorized into two types. The first type is referred to as land-cover modification where subtle changes affect the character of the land-cover without changing its overall classification, such as drought and burned areas within natural vegetation [14]. Land-cover modification is often associated with natural climate variability. The second type of land-cover change is referred to as land-cover conversion where there is a complete replacement of one land-cover type by another such as the transformation of natural vegetation by agriculture.

Change detection methods have been extensively reviewed by Lu and Weng [15] as well as Coppin *et al.* [14]. The majority of the methods that were reviewed by the aforementioned authors are based on image differencing, post-classification comparison and change trajectories of multi-date high resolution data. In most cases, these methods only consider two images for change detection, effectively trying to detect areas of change from one image to the next. Coarse resolution satellite data provide frequent observations (daily or multi-day composites) of land surface conditions at regional to global scales and are thus an attractive option for regional-scale change detection. Many change detection methods based on high-frequency, coarse resolution satellite data do not rely on true time-series analysis. The data are mostly treated as hyper-dimensional or as derived metrics [16–19] but not as hyper-temporal, failing to exploit the valuable temporal components, for example, the phase or frequency modulation of the signal, which is driven by seasonal changes in land surface phenology [20]. In addition, many of these methods consider large-scale ecosystem disturbances, for example, wildfires, insect outbreaks and natural disasters [18, 19] as opposed to the relatively small spatial extent of a new settlement development which involves but a few contiguous MODIS pixels.

As stated in the previous section, the most pervasive form of land-cover change in South Africa is human settlement expansion. Consequently, developing a change detection framework for detecting the formation of new settlements using a remote sensing approach will be the point of departure towards

the greater objective of developing a global or regional automated land cover change detection method. It follows that the primary objective of this thesis is to develop and test an automated change detection framework that is able to detect the transformation of natural vegetation to human settlement which could then be adapted to consider many other types of land cover change. Two novel change detection methods were formulated to solve the aforementioned problem. Both of these methods utilize the hyper-temporal time-series data that are available from coarse resolution imagery. The novelty of these methods is underpinned by the fact that the temporal dimension of the time-series is considered as a highly sampled (relative to the natural phenological variation) data-stream, and change classification is done by combining standard signal processing based methods for feature extraction with machine learning methods for change classification.

1.3 PROPOSED SOLUTION

As stated previously, change detection methods are required to be sufficiently automated with minimal operator involvement. Machine learning enables computers to make decisions based on volumes of empirical data that are often impossible to analyze in a timeous manner by a single, or even multiple human operators. When considering the use of machine-learning methods for change detection based on remote sensing data, there are a few factors to consider. Firstly, a change metric needs to be calculated. This change metric should effectively quantify the level of change that is associated with each pixel. This change metric is then compared to a threshold value to determine whether a change or no-change decision should be made [21], [22], [23]. The threshold value can be calculated in a supervised or unsupervised manner. In supervised methods, training data are used to determine the distribution of the change metric for both the change and no-change case and an appropriate decision boundary is inferred. One of the main disadvantages of supervised change detection methods is the requirement of a statistically significant *a-priori* database of change and no-change examples [8]. Unsupervised methods, on the other hand, do not require any training data, but this generally comes at the cost of a loss in performance.

In many cases, Univariate Image Differencing (UID) is used [24] to determine the change metric by subtracting two spatially-registered high resolution images, acquired at two different instances, on a per-pixel basis. Each pixel is then classified as either belonging to the change or no-change class by comparing the difference of two co-located pixels (change metric) to a threshold value. The underlying idea is that no-change pixels would typically have a smaller difference than change pixels, and a simple thresholding approach can be used to distinguish between the two possible classes. The selection of this single threshold value is, however, not a trivial task [23, 25, 26], especially when

considering an unsupervised approach. In most cases, the change metric Probability Density Function (PDF) is assumed to be normally distributed [22, 23] (See section 5.4 for details).

The specific sensor that was considered in this thesis is the MODIS sensor on-board the Terra and Aqua satellites. In particular, the freely available and easily accessible MCD43A4 product was used [27]. This product utilizes MODIS data from both satellites and provides high quality 500-meter reflectance data. A bidirectional reflectance distribution function (BRDF) is used to model the values as if they were taken from nadir view [28] which ensures a high level of consistency when considering the hyper-temporal time-series (see section 2.5). Even though some MODIS products are produced at 250 m resolution for the first two bands [27], these products are unfortunately not BRDF corrected and also only use data from either the Terra or Aqua satellites, and do not capitalize on both. Eight day composites are produced from daily data in an attempt to create the most cloud free, high quality dataset. Using this 8-daily composited dataset, a seven-year hyper-temporal time-series of surface reflectance was constructed (Jan. 2001 – Jan. 2008) and consequently used to detect the formation of new human settlements in South Africa. The underlying idea is that one or more hyper-temporal time-series be used as input to a change detection algorithm. The output of the algorithm is a change alarm which produces a change or no-change decision on a per-pixel basis.

To achieve this goal, two change detection methods are proposed in this thesis. The first will be referred to as the Extended Kalman Filter (EKF) change detection method and the second the Temporal Autocorrelation Function (ACF) change detection method. These methods work on a change metric thresholding principle, i.e. a pixel's hyper-temporal time-series is used to calculate a change metric. This change metric is then compared to a threshold value which yields a change or no-change decision. As previously stated, determining a suitable threshold is not a trivial task. A logical approach in selecting this threshold would be to calculate the change metric for a hyper-temporal times-series dataset of change and no-change examples. A threshold value can then be chosen that best discriminates between these two datasets. The problem with this approach is that real change examples are very rare in a regional landscape [17], which makes the availability of a training dataset on change problematic. This requires a new approach to the problem. The fact that real change examples are very difficult to obtain implies that no-change examples are relatively easy to obtain. Land cover change was therefore simulated [29]. This was done by linearly blending a natural vegetation time-series with that of a settlement time-series (for details see section 5.2.2). This enabled the timing and rate of the change to be controlled in order to estimate the necessary threshold parameters without the need for real change examples.

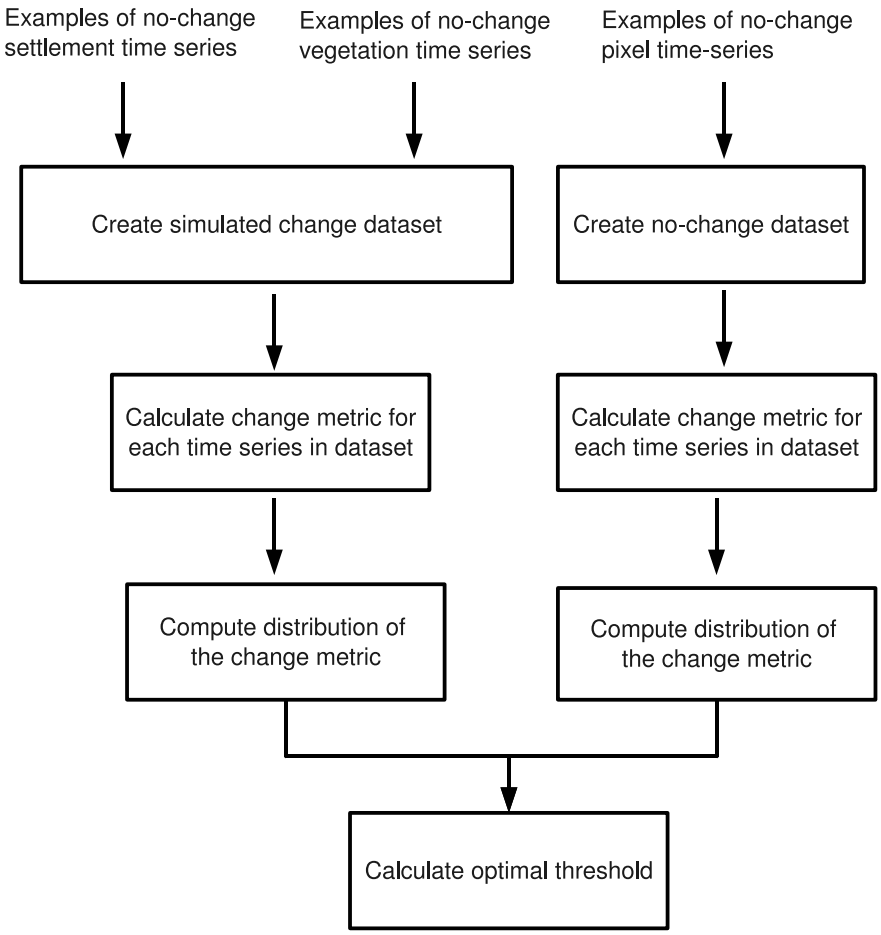

FIGURE 1.2: Off-line optimization phase.

Both the EKF and Temporal ACF change detection methods are supervised, however, the operator only needs to provide examples of "no-change" natural vegetation and settlement pixels. No real or actual change examples are required except for final performance evaluation. As previously stated, the training database requirement for both methods is limited to only no-change examples, which are numerous and can be obtained in large numbers. The no-change examples are then used to generate a simulated change dataset. Both the no-change and simulated change datasets are then used to determine a set of parameters in an off-line optimization phase after which the algorithm is run in an operational and unsupervised manner for the entire study area.

Figure 1.2 shows a general overview of the off-line optimization phase, which is similar for both methods. A set of settlement and natural vegetation time-series examples known not to have changed during the study period is used to create a simulated change dataset. The change metric for each time-series in the simulated change dataset, as well as the no-change dataset, is calculated. The change

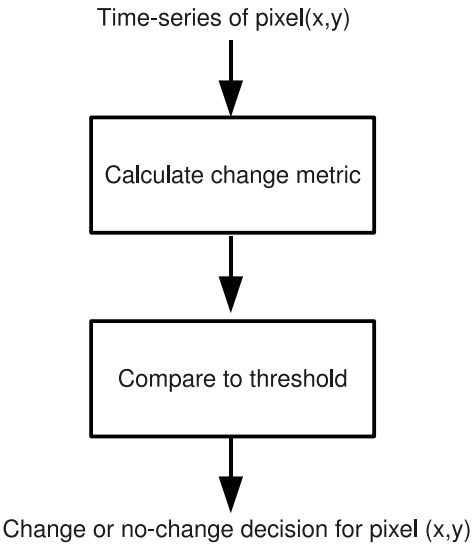

FIGURE 1.3: Operational phase.

metric is merely an index that indicates the amount of change that is associated with the time-series under consideration, i.e. the larger the change metric value, the higher the probability that the specific time-series had undergone a change. The distribution of the change metric, given that a change occurred together with the distribution of the change metric, given that no change occurred, is then used to calculate the optimal threshold.

Figure 1.3 shows a general overview of the operational phase, which is also similar for both methods. The time-series for any arbitrary pixel is used as an input to the algorithm. The change metric is then calculated and compared to the threshold that was calculated in the off-line optimization phase. After thresholding, a change or no-change decision is made. Even though the change detection methodology for both of the proposed change detection methods is similar, the change metric calculation is considerably different; this will become more apparent in the chapters to follow (Sections 5.2 and 5.3)

1.4 OUTLINE OF THIS THESIS

The outline of the thesis is as follows: Chapter 2 gives an overview of some basic remote sensing principles and describes the remotely sensed data that were used, together with an overview of some of the most common change detection methods found in current literature. Chapter 3 gives an introduction to non-linear filtering and in particular the Extended Kalman Filter (EKF), which is a crucial component of one of the proposed change detection methods. Chapter 4 shows that land-cover

class separation can be improved by modeling a normalized difference vegetation index (NDVI) time-series using a triply modulated cosine function and EKF framework to track the model parameters. Chapter 5 follows on the methodology discussed in chapter 2 and extends the EKF framework to the change detection case. The temporal Autocorrelation Function (ACF) change detection method is also introduced in chapter 5. The results obtained by using the EKF and temporal ACF methods are shown in chapter 6. Chapter 7 gives concluding remarks as well as possible future research that could expand on some of the concepts introduced in this thesis.

CHAPTER TWO

REMOTE SENSING DATA FOR LAND-COVER CHANGE DETECTION

Remote sensing is the science of obtaining information about an object or area without being in contact with the object or area under investigation [11]. Using various sensors, data are acquired remotely and analyzed to obtain information about the object that is measured by the sensor. In this thesis, a sensor on board a satellite platform measures the reflection and emission of electromagnetic radiation by the Earth's surface at regular time intervals and these data are then used to infer changes in surface reflectance caused by land cover change.

The objective of this chapter is to give the reader insight into some of the basic principles of satellite remote sensing. A brief history of remote sensing is given in section 2.1 after which the fundamental principles of electromagnetic radiation as well as the interaction of electromagnetic radiation with the atmosphere and Earth's surface is discussed in section 2.2. The concept of resolution in the spectral, temporal, radiometric and spatial context is introduced in section 2.3. The factors considered in choosing a remote sensing system is given in section 2.4 where-after the MODIS sensor is described in section 2.5. Two vegetation indices are discussed in section 2.6 where-after a review of some of the popular change detection methods is presented in section 2.7. Concluding remarks are given in section 2.8.

FIGURE 2.1: The oldest surviving aerial photograph taken by James Wallace Black in 1860 over the city of Boston [11].

2.1 EARLY HISTORY OF REMOTE SENSING

The invention of photography in 1839 was an important first step towards space-borne remote sensing as we know it today. The first known aerial photograph was taken in France by Gaspard Felix Tournament over Bievre, France, but unfortunately those photographs no longer exist [11]. The oldest surviving aerial photograph is one of Boston, taken by James Wallace Black in 1860 (Figure 2.1). The first platforms used for aerial photography were tethered balloons. It was only during the First World War that aircraft were used as platforms for aerial photography to obtain information regarding troop movements, supplies and the effects of bombardments [30]. The use of remote sensing for environmental purposes only became more popular after the Second World War. The technological advances made on airborne camera design during the war were put to civilian use for terrain mapping and assessment. The use of aircraft for remote sensing purposes proved to be expensive and provided data for relatively small areas. The space programs of the 1960s ushered in a new age of remote sensing, using a satellite platform. Satellite technology advanced greatly during the 1960s mainly because of the space race between the USA and former USSR [30]. This new phase of remote sensing can be considered in four broad categories, namely military reconnaissance, manned space flight, meteorological satellites and earth resource satellites. Each of these categories will be explained in more detail in the following sections.

2.1.1 Military reconnaissance satellites

Prior to 1960, aerial photography was mainly used by the United States and the former USSR to monitor each other's military capabilities. In 1958, the possibility of using satellite for military reconnaissance was proposed at the Surprise Attack Conference in Geneva [30]. The first US space observation satellites, which were used for military reconnaissance, were within the CORONA, ARGON and LYNARD programs of the 1960s [30]. These missions were typically very short with any one mission not being more than one or two weeks. These early systems were limited because of the finite amount of film that could be carried. The film canister was ejected and intercepted as it descended to Earth [30]. Later systems stored images in digital format and used telemetry to relay the data to the Earth.

2.1.2 Manned space flight

The first person to orbit the Earth was Yuri Gagarin on 12 April 1961. Even though no photos were taken during this flight, the potential for space-based earth observation became apparent. The USA also commenced its manned space programs in the early 1960s which culminated in the first lunar landing in 1969 [30]. The Mercury program (1961–1963) produced some of the first photographs from a manned capsule and was obtained by the astronauts through the capsule window. The Gemini program in later years (1965–1966) had a more systematic photograph acquisition strategy which captured more than 2 500 photos of the Earth. The Skylab missions (1973–1974) obtained over 44 000 images of the Earth at a spatial resolution of 60–140 m. The space shuttle missions that began in 1981 employed even more sophisticated remote sensing systems. The Russian space missions paralleled those of the American missions, with the Vostok and Voskhod programs being analogous to the Mercury and Gemini missions [30].

Using manned spacecraft as a remote sensing platform has both advantages as well as disadvantages. One of the main advantages is that the manned mission can be used as a test bed for new systems. By using feedback from the ground station, the on-board equipment setup can be modified and optimized by the astronauts. This information can then be used when designing an unmanned satellite. The astronauts could also rectify certain malfunctions with the sensors if and when required. The disadvantage, however, is that manned space missions are more often than not of short duration, which makes continuous and systematic coverage impossible. Another disadvantage is that the ramifications of malfunctions during a manned space mission far outweigh that of an unmanned satellite mission due to possible risk to human life.

2.1.3 Meteorological satellites

Weather forecasting relies heavily on remote sensing satellites to provide readings on temperature, wind speed and the location and movements of storms to name but a few. The movement of major hurricanes can be tracked and predicted accurately by using remote sensing images and can be relayed to the community effectively by means of radio and television broadcasting. Before the advent of remote sensing for weather prediction purposes, major storms could strike unexpectedly, causing massive damage to property and, quite possibly, loss of life. The Television and Infrared Observation Satellite (TIROS-1) meteorological satellite was the first that was used for earth observation and was launched by the United States on 1 April 1960 [30].

Since the initial TIROS-1 satellite, weather satellites have become increasing more advanced. Infrared (IR) data are used to determine information on the temperature at the surface and cloud tops and estimating wind direction and strength by monitoring individual clouds over time. Both polar orbiting and geostationary satellites are utilized for weather prediction [30].

2.1.4 Earth resources satellites

The first earth observation satellite was the Earth Resource Technology Satellite (ERTS-1) launched in July 1972. The ERTS-1 (commonly referred to as Landsat) was designed to acquire multi-spectral medium resolution imagery of the Earth on a systematic and repetitive basis [30]. The data acquired during this mission were made available globally. The underlying idea was that the global remote sensing community would take part in evaluating the subsequent data. The mission was regarded as being very successful and paved the way for continuation of the Landsat series of satellites. The first radar satellite used for remote sensing purposes was the SEASAT satellite, which was launched in 1978 but only provided data for three months. Prior to 1980, the majority of satellites were deployed by the USA and USSR. During the 1980s and onwards, remote sensing systems were developed and commissioned from various agencies around the world, including the French Satellite Pour l'Observation de la Terre (SPOT) series of satellites, the range of Indian Remote Sensing (IRS) satellites, the Japanese Earth Resource Satellite (JERS) and the European Remote Sensing (ERS) satellites to name but a few.

Typically, these space agencies operate independently of one another but in in February 2005 the Group on Earth Observations (GEO) was formally created by resolution of 60 national governments and 40 international organizations. The nations and international organizations involved in GEO resolved that it would implement the Global Earth Observation System of Systems (GEOSS). The primary objective

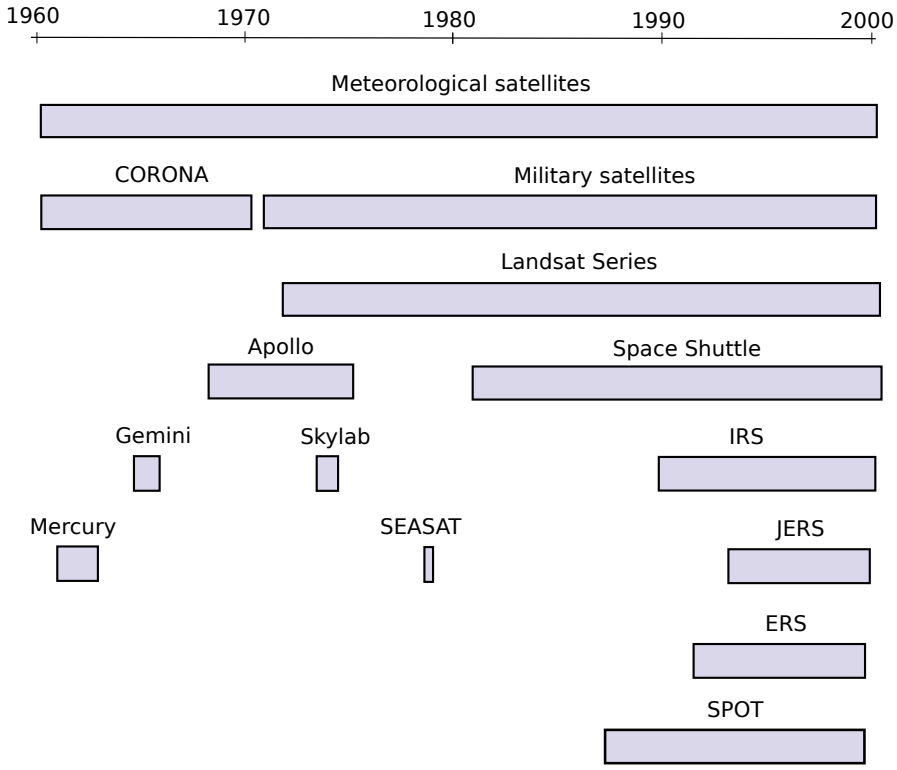

FIGURE 2.2: Time-line spanning from 1960 until 2000 for some of the satellite missions described in the previous sections. Since the first artificial satellite, Sputnik 1, in 1957, a host of nations have successfully launched more than 2 000 satellites into orbit. (Adapted form [30])

of GEOSS is that that timely, quality, long-term, global observations are exchanged in a full and open manner with minimum time delay and minimum cost. They also intend to coordinate efforts to address capacity-building needs related to earth observations [31].

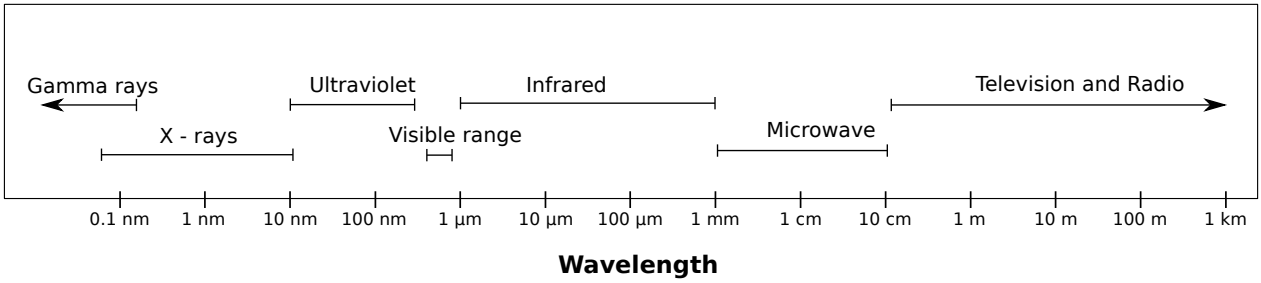

FIGURE 2.3: The electromagnetic spectrum [30].

2.2 ELECTROMAGNETIC RADIATION

Visible light is probably the most familiar form of electromagnetic radiation, but only occupies a very small portion of the entire electromagnetic spectrum. Radio waves, X-rays and Ultra Violet (UV) rays, to mention a few, all form part of the electromagnetic spectrum. In essence, all forms of electromagnetic radiation radiates according to the same wave theory. These waves are characterized by their wavelength and amplitude, all traveling at the speed of light in a vacuum. The electromagnetic spectrum is depicted in Figure 2.3.

The two main approaches to remote sensing are active and passive systems. An active remote sensing system uses its own electromagnetic radiation source. The amount of energy that is reflected back to the sensor is used to infer information about the surface towards which the sensor is directed. A typical example of an active remote sensing system is Synthetic Aperture Radar (SAR). These systems operate in the wavelength range of between 2.4 and 107 cm.

A passive remote sensing system uses the Sun as the source of electromagnetic radiation and measures the reflection from the Earth's surface. The focus of this thesis will be on passive remote sensing systems. The part of the spectrum that is particularly useful for passive remote sensing systems are the visible and infrared (IR) ranges. Table 2.1 gives a further breakdown of these ranges. Multi-spectral scanners often range between 0.4 and 12.0 μm range [11], which ranges from the visible blue range to the long-wave IR range (Table 2.1).

As previously stated, the Sun is the primary source of electromagnetic radiation in passive remote sensing systems. It follows that the properties of the Sun's electromagnetic radiation are of particular importance. Although the Sun produces energy in a wide range of wavelengths, the energy across all the wavelengths is not evenly distributed. Wien's displacement law dictates that the wavelength at which a black body radiates maximum energy is a function of the temperature of the object given

TABLE 2.1: Breakdown of the visible and infrared spectrum.

	Range	**Wavelength** (μm)
Visible	Blue	0.4 – 0.5
	Green	0.5 – 0.6
	Red	0.6 – 0.7
Infrared	Near IR	0.7 – 1.0
	Short-wave IR	1.0 – 3.0
	Mid-wave IR	3.0 – 5.0
	Long-wave IR	7.0 – 14.0
	Far IR	15.0 – 1000

as [30]:

$$\lambda_m = \frac{A}{T}, \tag{2.1}$$

where λ_m is the wavelength at which the maximum energy is radiated, A is a constant (2898 μm K) and T is the temperature in Kelvin. The Sun's temperature is between 5750 and 6000 K [30]. This implies that the wavelength at which the Sun radiates maximum energy is roughly 0.5 μm. The spectral radiance of electromagnetic radiation as a function of the temperature and wavelength is described by Planck's law [32]:

$$I(\lambda, T) = \frac{2hc^2}{\lambda^5(e^{\frac{hc}{\lambda kT}} - 1)}, \tag{2.2}$$

where λ is the wavelength, T is the temperature, h is the Planck constant, k is the Boltzmann constant and c is the speed of light. Figure 2.4 shows the spectral radiance of the electromagnetic radiation of the Sun for wavelengths between 1 and 2000 nm. It can be seen that the Sun's maximum energy is radiated in the visible spectrum between 400 and 700 nm.

Because of the distance between the Earth and Sun, there is a considerable decrease in intensity across all wavelengths when the electromagnetic radiation reaches the Earth's atmosphere. This can be attributed to the inverse-square law that states that flux density is inversely proportional to the square of the distance from the flux source [32]. However, the spectral distribution across the wavelengths remains nearly unchanged [30]. The atmosphere, on the other hand, has a dramatic effect on the solar radiance that eventually reaches the surface of the Earth. This effect will be discussed in the following

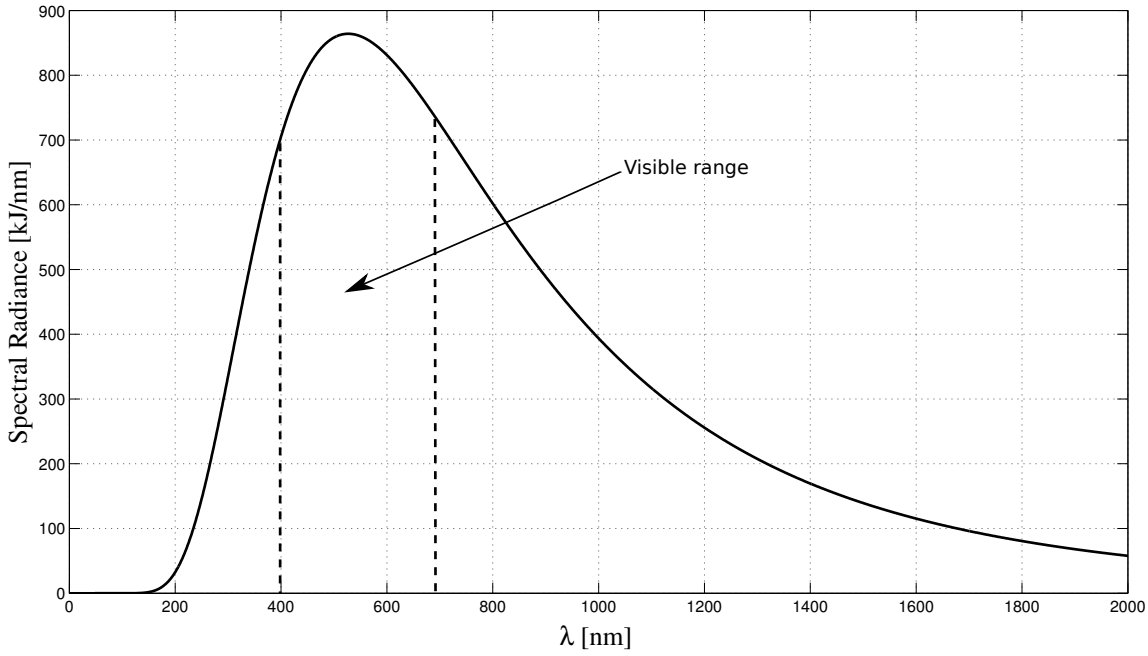

FIGURE 2.4: Solar spectral radiance of the Sun as a function of wavelength.

section.

2.2.1 Interaction of electromagnetic radiation with the atmosphere

The atmosphere has a significant effect on the intensity and spectral composition of electromagnetic radiation that is available to remote sensing systems. The influence of the atmosphere can be partitioned into scattering effects and absorption effects.

Scattering can either be selective or non-selective. Selective scattering depends on the specific wavelength of the radiation. If the wavelength of the electromagnetic radiation is larger than the dimensions of the scatterers (more than 10 times the size), the amount of scattering is inversely proportional to the fourth power of the wavelength [30]. This is commonly referred to as Rayleigh scattering. When the dimensions of the scatterers are approximately the same as the wavelength of the electromagnetic radiation, scattering also occurs. This is commonly referred to as Mie scattering. Non-selective scattering is not wavelength dependent and occurs in aerosols that are approximately 10 times the size of the wavelength. For the visible wavelengths, pollen grains, raindrops and cloud droplets are typical sources of non-selective scattering [30].

Absorption in the atmosphere occurs because gaseous components in the atmosphere act as selective

Table 2.2: Order of magnitude of atmospheric effects for Advanced Very High Resolution Radiometer (AVHRR) band 1 and 2 as well as NDVI. The proportional effect is given as percentage (%) of increase (+) or decrease (-) of the signal. All the other effects as well as effect on NDVI are given in absolute units [33].

	Ozone	**Water vapor**	**Rayleigh**	**Aerosol**
Band 1	4.24% to 12% (-)	0.7% to 4.4% (-)	0.02 to 0.06 (+)	0.005 to 0.12 (+)
Band 2	–	7.7% to 25% (-)	0.006 to 0.02 (+)	0.003 to 0.083 (+)
NDVI (Bare Soil)	0.02 to 0.06 (+)	0.011 to 0.12 (-)	0.036 to 0.094 (-)	0.006 to 0.085 (-)
NDVI (Forest)	0.006 to 0.017 (+)	0.036 to 0.038 (-)	0.086 to 0.23 (-)	0.022 to 0.35 (-)

absorbers [30]. Molecules selectively absorb energy at different wavelengths. The most efficient absorbers in the atmosphere are water vapor, carbon dioxide and ozone [11]. Figure 2.5 shows the atmospheric electromagnetic opacity for different wavelengths. Table 2.2 shows the effect for AVHRR band one and two as well as NDVI as a result of Ozone, water Vapor, Rayleigh scattering and stratospheric aerosol effects. Both AVHRR band one and two are affected by these atmospheric effects and in particular, water vapor and aerosol has a detrimental affect on band 2 and 1 respectively which causes an artificial decrease in NDVI [33] (Table 2.2).

From the aforementioned it can be concluded that, because of the effects of atmospheric absorption and scattering, the observation radiance recorded at the satellite is not a true reflection (NPI) of the radiance from the ground but rather “Top-of-Atmosphere”. It follows that atmospheric correction for Rayleigh scattering, gaseous absorption, and aerosol scattering should be a critical pre-processing step when considering land surface studies [34, 35]. For three cases in particular, the omission of atmospheric correction could prove to be detrimental [36]. Firstly, if one were to compute the ratio between two bands of a multispectral image. This is because scattering increases inversely with wavelength which implies that shorter-wavelength measurements are more susceptible than longer-wavelengths and could possibly distort the true ratio. Second, when relating the radiance of a surface in terms of a physically based model, the atmospheric component must be estimated and removed as failure to do so could adversely affect the physically based model if the physically based model does not assume an atmospheric component. Thirdly, when comparing the radiance made at one time (time 1) with the radiance at a different time (time 2), atmospheric correction is crucial as the radiance values recorded by the sensor will most likely vary from time 1 to time 2 because of atmospheric variability [36]. Atmospheric correction is also applicable to time-series analysis

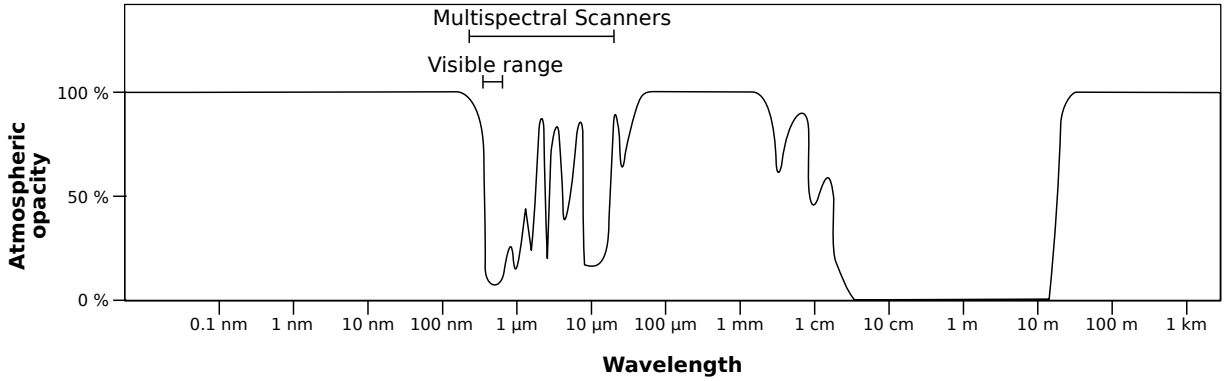

FIGURE 2.5: Atmospheric electromagnetic opacity (modified from [37]).

(considering multiple observations of the same area) as changes in the time-series should only be affected by changes in the surface radiance as opposed to changes in atmospheric conditions.

Atmospheric correction can either be relative or absolute. Relative atmospheric correction uses histogram matching to reference images. This approach requires good reference images for the same or adjoining areas. Absolute correction on the other hand can either be empirical or physical. Empirical methods have the danger of over simplification and are often of limited use. Physical models model the effect of various gas concentrations and compensates for these accordingly. These physical modes are called Radiative Transfer Models (RTM's). Radiative transfer models rely on information from the image itself in order to estimate the path radiance for each spectral band and are limited by the need for data relating to the condition of the atmosphere at the time of imaging. A popular RTM is the 6S code developed by E Vermote *et al.* [38] and is freely available (ftp://loa.univ-lille1.fr/6S/).

2.2.2 Interaction of electromagnetic radiation with a surface

When electromagnetic energy strikes a surface, a certain measure of absorption, reflection and/or transmission can occur. The amount of energy reflected, absorbed and transmitted is a function of the Earth feature (material composition, surface roughness, etc.) and the wavelength of the electromagnetic energy concerned. In remote sensing, the energy that is reflected from the surface is of particular importance as this is the energy that is detected by the sensor. Reflection is primarily a function of the surface roughness. If the surface is very flat, and the angle of reflection (θ_r) equals the angle of incidence (θ_i), most of the energy will be reflected in the direction of the reflection angle. This type of reflection is referred to as *specular* reflection. If the surface is rough compared to the wavelength of the incident electromagnetic radiation, i.e. the ratio between the roughness of the surface and the wavelength is greater than one, the energy is scattered and effectively reflected in all

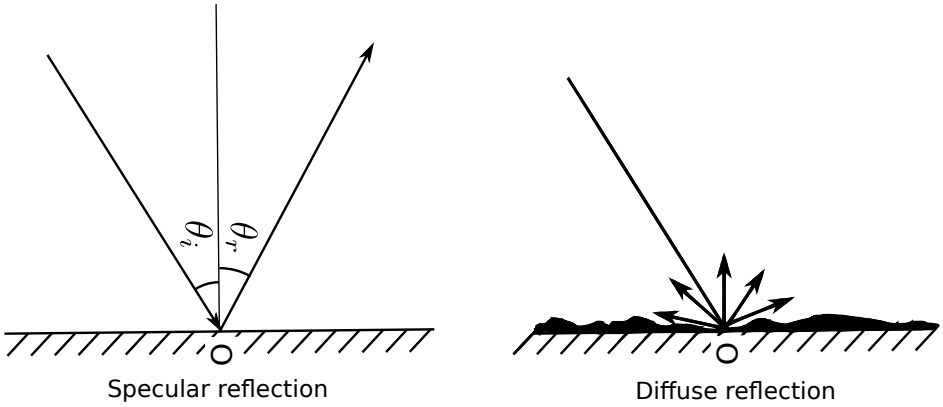

FIGURE 2.6: Specular and diffuse reflection [30].

directions. This type of reflection is referred to as *diffuse* reflection [11]. The broad range of surface types on Earth implies that perfect specular or diffuse reflection would not occur in nature and would lie somewhere between these two extremes [11]. Figure 2.6 illustrated the principle of specular and diffuse reflection.

For remote sensing purposes, diffuse reflection is considered to be more favorable as the reflection is coherent for all viewing angles. Specular reflection, on the other hand, would have a bright reflectance for a specific viewing angle, and relatively little reflection for all other viewing angles. The reflection for most surfaces in nature tend to be more diffuse than specular for the visible and infrared wavelengths with the exception of water [30]. Because surfaces cannot be assumed to be perfectly Lambertian (diffuse reflection), the viewing and solar angles should be considered. All the reflected energy from a ground target over an entire hemisphere is not detected by the satellite sensor, but rather, only the reflected energy returned at a particular angle is recorded [36]. In addition, the reflected energy also depends on the the orientation of the Sun (Figure 2.7 and 2.8). These effects are particularly detrimental for wide-swath sensors [39] as the viewing angle of these sensors can vary considerably between days. The MODIS sensor, for example, has a swath width of approximately 2300 km, which yields a maximum viewing zenith angle of up to 65° [28]. It follows that the distribution of radiance as a function of the observation and illumination angles must be taken into consideration. The Bidirectional Reflection Distribution Function (BRDF) is a mathematical function that describes the variability in surface reflection based on the illumination and viewing angles for a specific wavelength. Using the BRDF function to correct for Sun and viewing angle effects is discussed in further detail in section 2.5 when considering the BRDF corrected MODIS product that was used in this study.

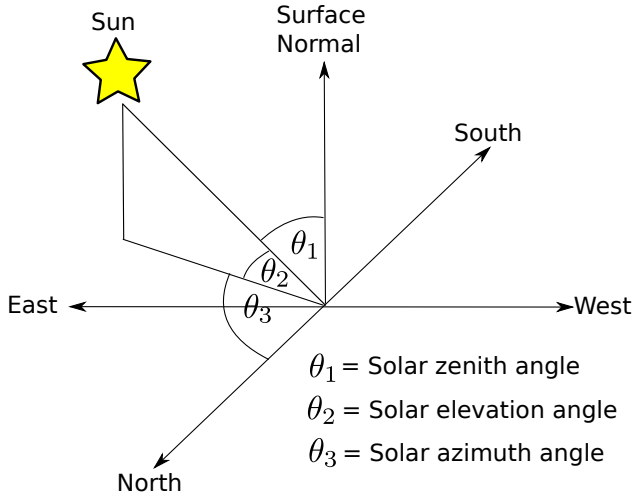

FIGURE 2.7: Solar orientation [36].

The spectral reflection is the ratio between the energy reflected from a surface and the total electromagnetic energy incident on the surface. The spectral reflectance (ρ_λ) is a function of the wavelength and can be written as

$$\rho_\lambda = \frac{E_R(\lambda)}{E_I(\lambda)} \times 100, \tag{2.3}$$

where E_R is the reflected electromagnetic energy and E_I is the electromagnetic energy incident on the surface [11].

The spectral reflectance curve of an object is a graph that shows the spectral reflection for a range of wavelengths. This is sometimes also referred to as the spectral signature of an object. Figure 2.9 shows an example of the spectral reflectance curve for vegetation. The typical valleys in the visible spectrum are due to the absorption characteristics at different wavelengths by the pigments in plant leaves. The strong absorption of chlorophyll in the blue and red band gives rise to the typical green color that is usually associated with healthy vegetation. Water absorption in the 1400, 1800 and 2700 nm band gives rise to the characteristic valleys in the short-wave IR region. As explained in section 2.2.1, water vapor in the atmosphere is an important consideration for atmospheric correction and has also been a limitation of previous land remote sensing instruments, in more recent sensors (for example MODIS), bands are chosen to minimize the impact of absorption by atmospheric gases and in particular water vapor [41].

FIGURE 2.8: Effect of Solar illumination angle variation on reflection [40]. Both photographs taken from the same field but from different directions.

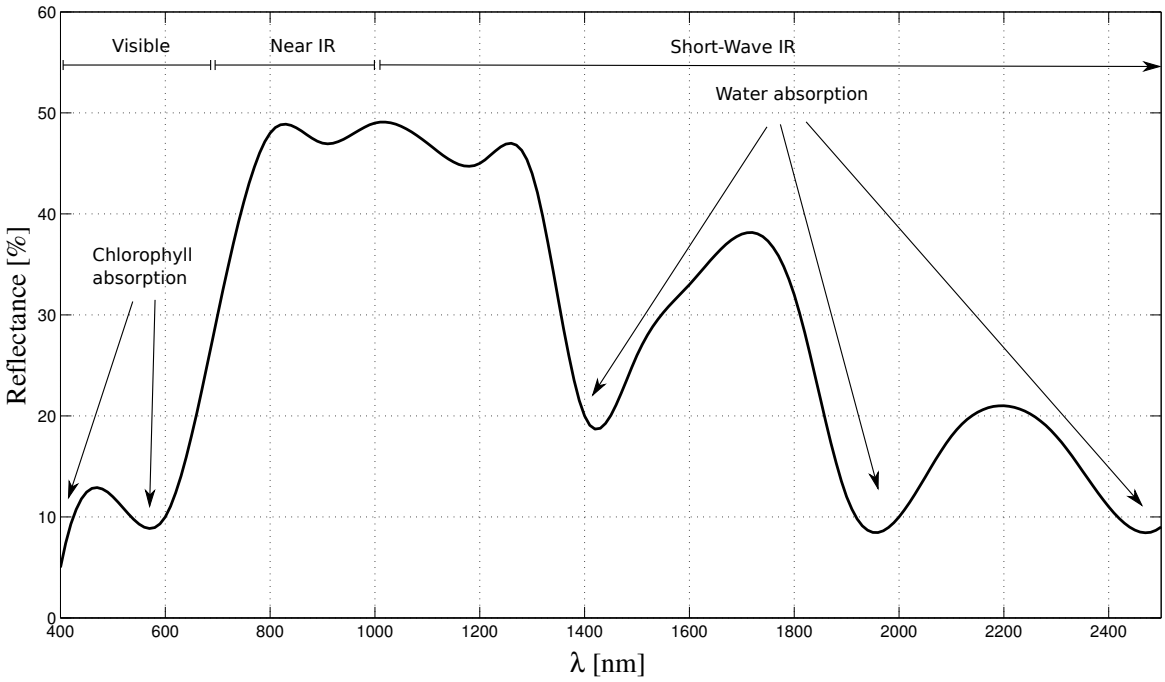

FIGURE 2.9: Typical spectral reflectance curve for vegetation [11].

2.2.2.1 Phenology reflection variation

Even though the spectral reflection curve is broadly similar for specific land-cover types, it is by no means unique. In nature, the spectral signature of similar land-cover types could be highly variable [11, 30]. Even the same land cover type can appear significantly different during certain periods of

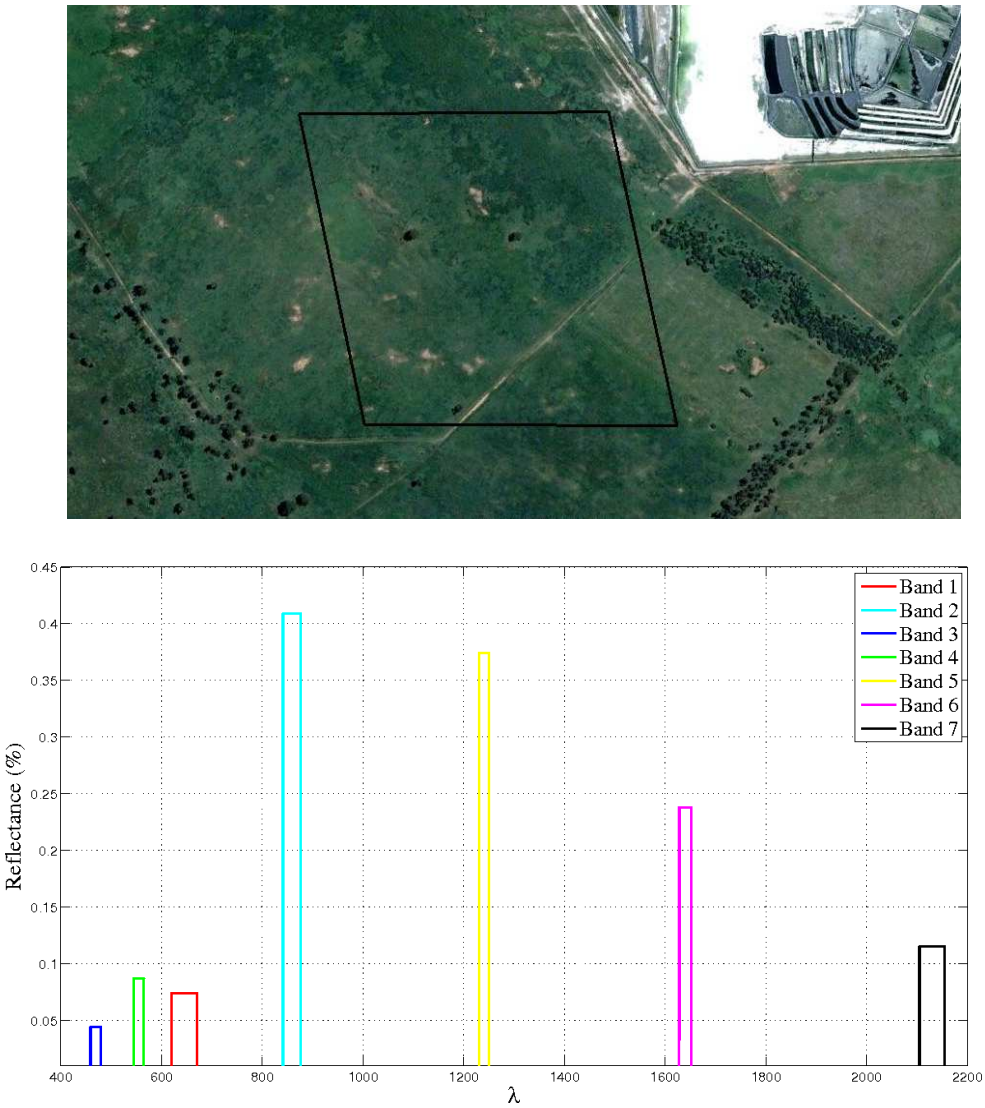

FIGURE 2.10: QuickBird image showing a vegetation area taken in February (courtesy of Google^{TM}Earth). The area corresponding to a 500 m MODIS pixel together with the the spectral reflection for all seven MODIS land bands is also shown.

the natural growth cycle. An example of this is shown in the Limpopo province of South Africa. A natural vegetation area corresponding to a 500 m MODIS pixel is shown together with the the spectral reflection of all seven land-bands for February and September respectively (Figures 2.10 and 2.11). It is clear that the spectral signature of a pixel having an unchanged land cover type could vary considerably over time due to seasonal variations. The Near IR band (band 2) in February is high and the red band (band 1) is low due to green vegetation whereas the opposite is true for September.

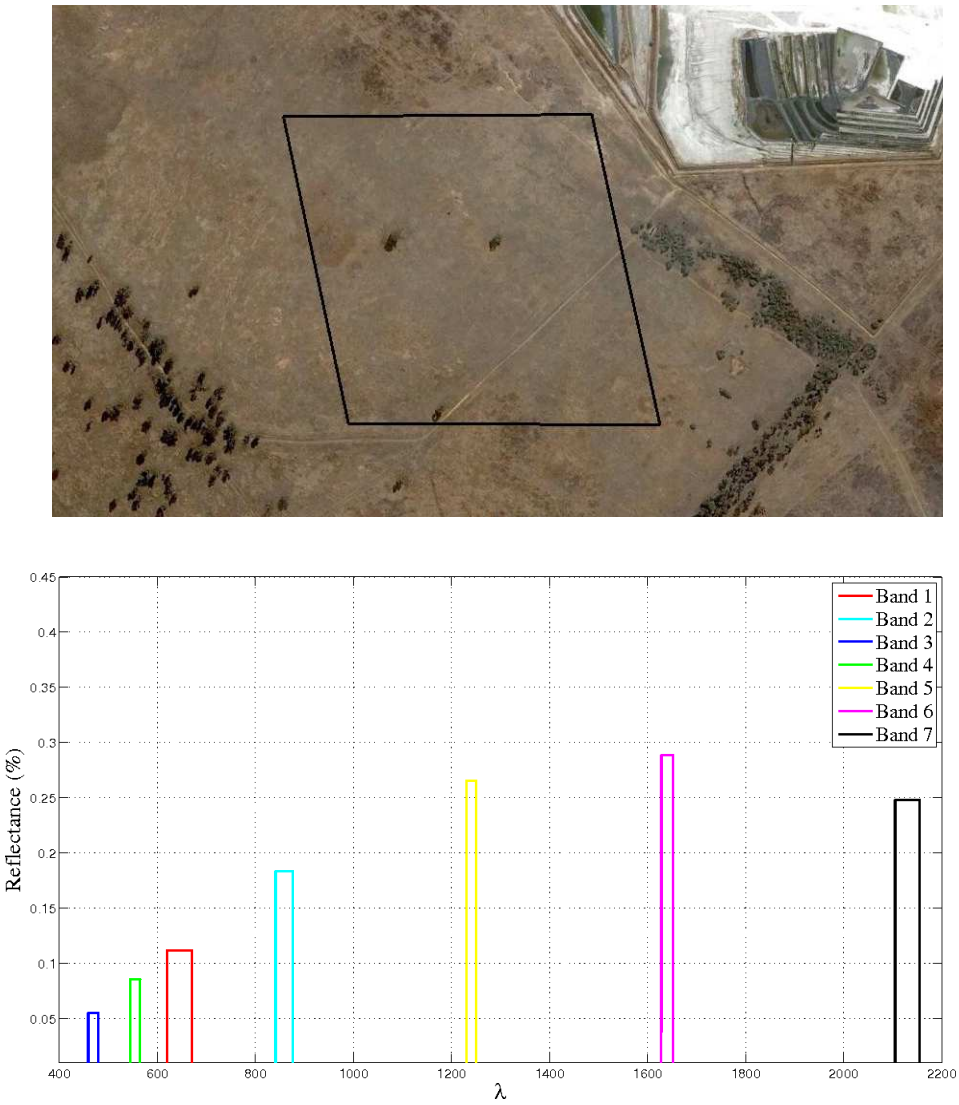

FIGURE 2.11: QuickBird image showing a vegetation area taken in September (courtesy of Google^{TM}Earth). The area corresponding to a 500 m MODIS pixel together with the the spectral reflection for all seven MODIS land bands is also shown.

2.3 RESOLUTION

In remote sensing, there are four types of resolution that are of interest. These are spectral, temporal, radiometric and spatial resolution. Each of these will be discussed in more detail in the sections that follow.

2.3.1 Spatial

The spatial resolution of an imaging system can be measured in a number of different ways, depending on the user's goals. The pixel size is determined by the altitude, viewing angle and sensor characteristics of the remote sensing system. The most commonly used measure, based on the

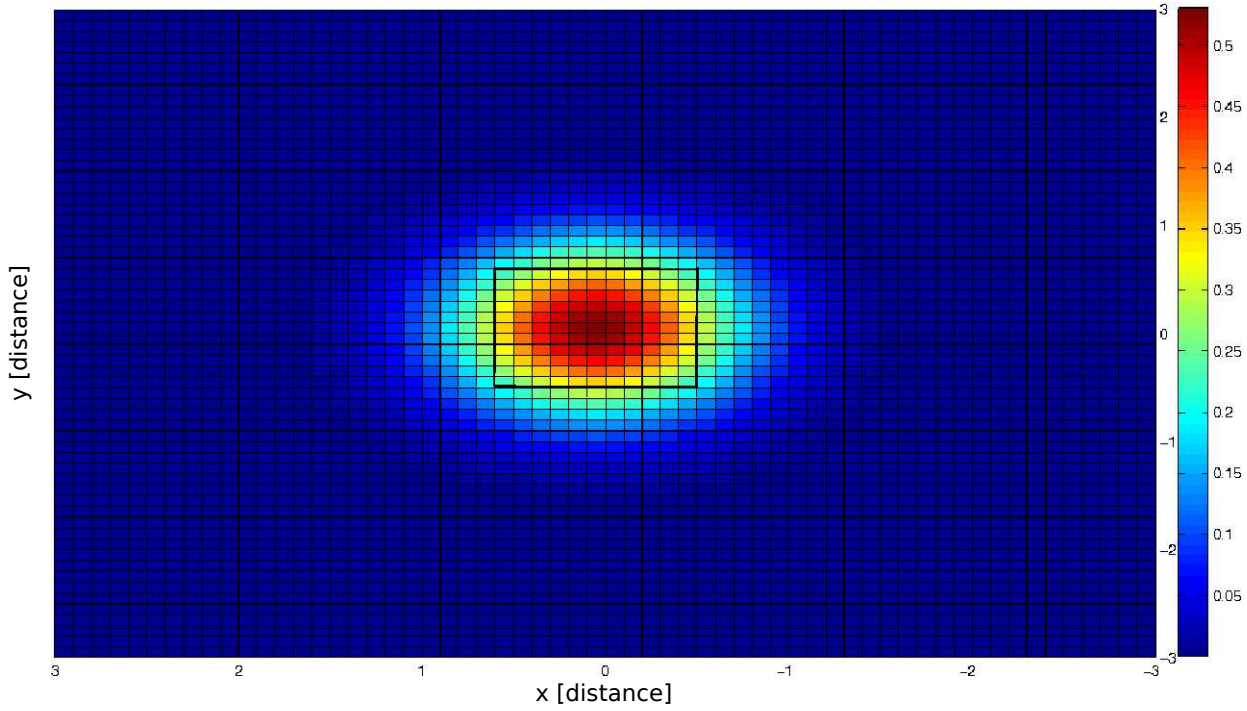

FIGURE 2.12: Illustration of the point spread function, the pixel that is imaged is centered at (0,0) and stretches from -0.5 and 0.5 in both the x and y direction [36].

geometric properties of the imaging system, is the instantaneous field of view (IFOV) which is defined as the area on the ground that is viewed by the instrument at a given altitude and time instance [36]. It should however be noted that no satellite has a perfectly stable orbit and the satellite's height above the Earth could vary by tens of kilometers which in turn influences the IFOV. Another factor to consider is that due to the properties of the optics involved in imaging, a reflective point on the ground does not produce a single bright point on the image but rather a diffused circular region. This phenomenon is characterized by the point spread function (PSF). Figure 2.12 illustrates the concept of the PSF, here, the area of the pixel being imaged is centered around (0,0) and stretches 0.5 in both the x and y direction. It is clear that the signal energy is non-zero outside this range. The ideal point spread function would be a square box centred at (0,0) with a side length of 1.0 [36]. When relatively bright or dark objects are within the IFOV of the sensor, the PSF has the effect of blending or spreading the areas having significantly higher or lower reflectance. This leads to the phenomenon where high-contrast features such as narrow rivers and roads are discernible on some satellite images, even though their width is less than the sensor's spatial resolution. It also has the effect that often, targets with dimensions larger than the satellites IFOV may not be discernible if they do not contrast with their surroundings. The value recorded at the sensor which corresponds with a particular pixel position on the ground is thus not just a average of the radiance from that pixel but there is a high probability that there is a contribution from areas outside the IFOV. A digital image is a set of values being related

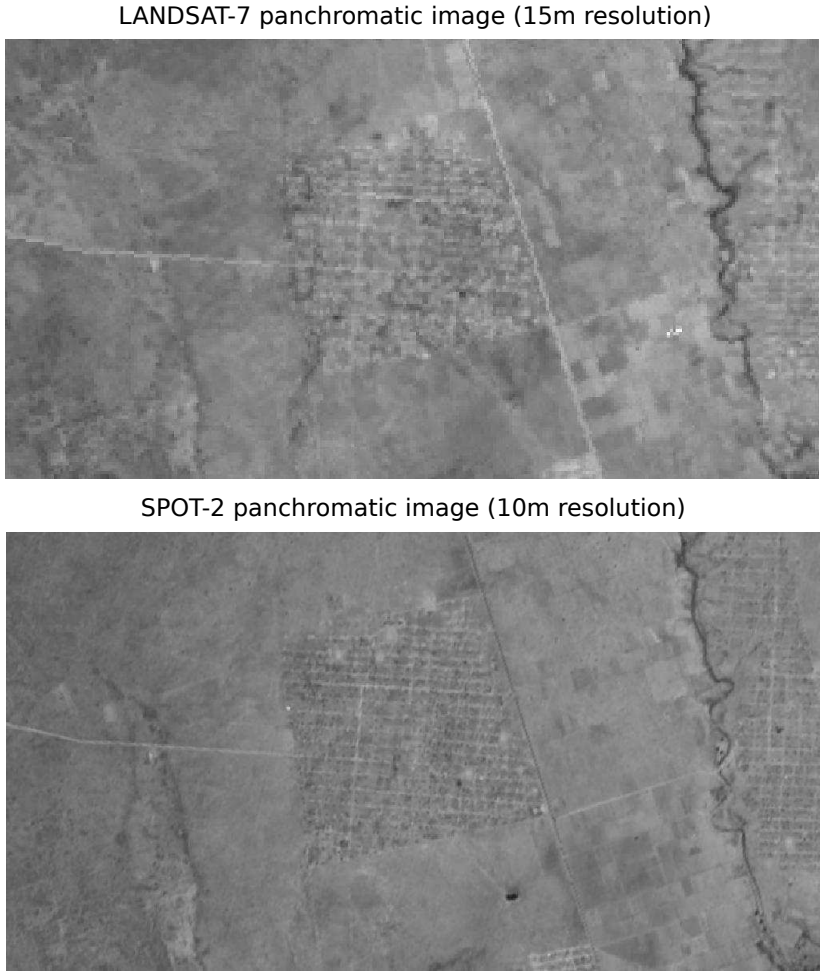

FIGURE 2.13: Landsat-7 and SPOT-2 panchromatic resolution comparison.

to the radiance from a ground area represented by a single cell or pixel. The IFOV is not the same as the pixel size as pixel values can be interpolated to represent any desired ground spacing [36].

When considering the same geographical area, a higher resolution image of the same area will have an increased data size when compared to a lower resolution image. An informal settlement in the Limpopo province of South Africa is shown in Figure 2.13, which was taken from the Landsat-7 and SPOT platforms respectively. The Enhanced Thematic Mapper (ETM+) sensor on board the Landsat-7 mission has a panchromatic channel with spatial resolution of 15 m, whereas the High-Resolution Visible (HRV) sensor on board the SPOT-2 mission has a panchromatic channel with a spatial resolution of 10 m. The distinct difference in clarity between the two images can be seen clearly when considering these two images of the same area.

2.3.2 Spectral

Remote sensing systems usually employ multi-spectral sensors. As the name suggests, multi-spectral sensors acquire data for multiple spectral bands. The effective bandwidth of the measured bands is directly related to the spectral resolution. For example, in the visible range between 400 and 700 nm, if only one band is used to sense the reflection for the entire band, a single reflectance value would be produced. If the one single band was divided into three sub-bands, namely 400–500, 500–600 and 600–700 nm respectively, three reflectance values corresponding to the blue, green and red band would be produced. One of the advantages of having a higher spectral resolution is that the variations in the spectral signatures of land surfaces can be identified much more easily as the spectral resolution increases. To identify particular targets on a remotely-sensed image, the spectral resolution of the sensor must be as closely matched as possible to the spectral reflectance curve of the intended target [36].

There are also a few drawbacks when increasing the spectral resolution. As the number of spectral channels increases, the data size increases linearly. Another disadvantage is that the Signal-to-Noise Ratio (SNR) is adversely affected when increasing the spectral resolution. The reason for this is that all signals contain some form of noise that is caused by electronic noise from the sensor. The effective signal radiance is less for narrow channels than for wider channels while the additive noise component remains the same, which in turn reduces the SNR. Some airborne sensors have more that 100 spectral bands. These sensors are referred to as hyper-spectral sensors. The sensors that were considered in this thesis typically had fewer than 10 land observation bands [36].

2.3.3 Temporal

Temporal resolution in remote sensing refers to the rate at which the same area is measured. The pre-determined orbit, altitude and swath-width of the satellite means that the rate at which an area is imaged can be determined. The orbital period of a satellite in a circular orbit increases with increasing altitude. Low earth orbit (LEO) satellites typically range between 160 and 2000 km above the Earth's surface and travel at a speed of nearly 8 km per second. Geostationary orbit ranges between 35488 to 36088 km, being centered on 35788 km and satellites in this orbit travel at speeds of around 3 km per second. The advantage of geostationary orbit is that the receiving antenna remains in a fixed position whereas the receiving antenna used to receive data from LEO satellites requires a tracking antenna. Many remote sensing satellites are in a sun-synchronous orbit (600 – 800 km) where the ground observation is always illuminated by the Sun at the same angle when viewed from the satellite [42]. The temporal resolution can vary from hours to weeks depending on the configuration of the remote

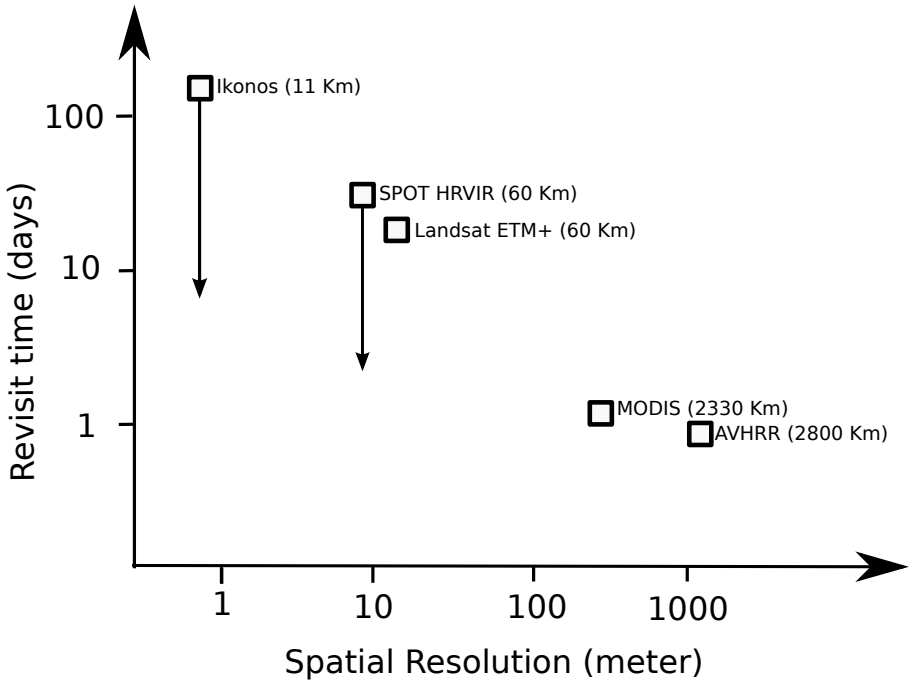

FIGURE 2.14: Relationship between image spatial resolution and satellite imaging revisit period. Instrument swath width is given in brackets and arrows show range of satellite imaging revisit period using sensor off-nadir pointing capability [43].

sensing system [30]. Fixed temporal resolution systems have a fixed viewing angle whereas the variable (off-nadir) viewing capabilities of later systems have the ability to alter the temporal resolution. The advantage of utilizing off-nadir viewing capability is that by changing the viewing angle slightly, the same area could be imaged on consecutive orbits. The disadvantage of this approach, however, is that while some areas can be imaged more frequently, other locations that may have been imaged from the same point are omitted which increases the revisit time for these areas [43]. In essence, fixed temporal acquisitions are not possible using variable viewing capabilities. The Ikonos sensor, for example, has a satellite repeat cycle of 140 days which can be increased to 3 – 4 days by making use of the pointing capability of the instrument. Crucially, imagery are thus only recorded based on user demand which implies that there is no regular repeated coverage for any part of the Earth's surface [43]. It should also be noted that there is a trade-off between spatial and temporal resolution of satellite data. The underlying idea is that the data from narrow swath instruments, having a finer spatial resolution, is less frequently available than wide swath sensors, having coarser spatial resolution data (Figure 2.14). The advantage of having equally spaced, frequently sampled acquisitions of the same area will become apparent in sections and chapters to follow.

2.3.4 Radiometric

Radiometric resolution refers to the number of digital quantization levels used to represent the data observed by the sensor. A higher quantization level usually implies a greater level of detail in the information that is collected by the sensor. If one were to consider a digital image composed of only two levels (black and white), each pixel could either be represented using a single bit with 0 representing black and 1 representing white. If we were to increase the number of bits to 6-bits, there would be 64 unique levels (000000_2 to 111111_2 in binary notation). It should be noted that the number associated with each quantization level is not a direct measurement of ground-leaving radiance but rather the steps into which a range of physical values is divided. Consider, for example, that the sensor is able to measure radiance in the range 0 to 10 $\mathrm{Wm^{-2}sr^{-1}}$ $\mu\mathrm{m^{-1}}$ and each pixel could be represented as an 8-bit value (i.e. 2^8=256 unique levels). The entire radiance range could be quantized in 256 levels with the difference between each level being (10 – 0)/255=0.00392 $\mathrm{Wm^{-2}sr^{-1}}$ $\mu\mathrm{m^{-1}}$. In an effort to distribute the incoming radiance more evenly over radiance range, some sensors can dynamically change their gain to maximize the resolution by taking into account the expected brightness conditions without saturating the detectors. The idea is that the gain can be lowered when surface brightness is expected to be high and increased when surface brightness is expected to be low.

The step size from one level to the next has to be more than the noise level of the sensor to ensure that the change in a level was caused by a real change in the radiance rather than a fluctuation in radiance caused by the noise. It follows that the SNR directly influences the quantization level. Low quality sensors having a high noise level would thus have a lower radiometric resolution compared with low noise sensors [36]. The disadvantage of increased radiometric resolution is an increase in the data size. Most remote sensing systems have 6 or more bits of radiometric resolution [30].

2.4 CHOOSING A REMOTE SENSING SYSTEM

Since the beginning of the remote sensing era, remote sensing satellite data have provided researchers with an effective way to monitor and evaluate land-cover changes [8, 14, 44]. A wide spectrum of sensors can be utilized for change detection and the focus is typically on the application requirement when selecting the most appropriate sensor.

When selecting the right sensor for detecting land cover conversion, the most important consideration is the spatial and temporal resolution. High resolution sensors have the advantage of identifying much smaller objects than coarse resolution sensors, but at a much lower temporal resolution. Change

TABLE 2.3: Comparison of remote sensing satellite sensors.

Sensor	Revisit time	Swath Width	Spatial Resolution	Wavelength range	No. of bands
Advanced Space borne Thermal Emission and Reflection Radiometer (ASTER)	16 Days	60 km	15 – 90 m	0.52 – 11.65 μm	14
Enhanced Thematic Mapper Plus (ETM+)	16 days	185 km	15 – 60 m	0.45 – 12.5 μm	8
MODerate-Resolution Imaging Spectroradiometer (MODIS)	1–2 days	2330 km	250 – 1000 m	0.4 – 14.4 μm	36
Advanced Very High Resolution Radiometer (AVHRR)	Daily	3000 km	1100 m	0.58 – 12.5 μm	5

detection is possible by comparing two high resolution images taken at different dates, but this can, however, be problematic, because similar land cover types can appear significantly different at various stages of the natural growth seasonal cycle [17]. To mitigate this problem it was shown by R.S Lunetta *et al.* in [45] and [46] that the temporal frequency of the remote sensing data acquisitions should be high enough to distinguish change events from phenological cycles [45, 46]. The high temporal frequency makes the use of coarse spatial resolution imagery very attractive for change detection [16].

To illustrate this, two narrow-swath and two wide-swath sensors typically used in land-monitoring remote sensing applications are shown (Table 2.3). The first two examples, Advanced Space-borne Thermal Emission and Reflection Radiometer (ASTER) and ETM+ each have a maximum panchromatic spatial resolution of 15 m with a swath width of 60 and 185 km respectively. The pair of examples, MODerate-Resolution Imaging Spectroradiometer (MODIS) and Advanced Very High Resolution Radiometer (AVHRR) have a much lower spatial resolution (250 m–1100 m) but with a much wider swath width of 2330 and 3000 km respectively. The wide swath width enables the same pixels to be sampled nearly every day and as such provides a very high temporal resolution.

The MODIS sensor was chosen for this thesis because of its wide swath-width and medium spatial resolution capabilities. The following section describes the MODIS sensor in more detail.

2.5 MODERATE-RESOLUTION IMAGING SPECTRORADIOMETER

MODIS was developed by NASA for scientific purposes and is the principal sensor on board the Terra and Aqua satellites. Terra, also commonly referred to as EOS-AM-1, was launched on December 18, 1999 from the Vandenberg Air force base. Development of the Terra satellite was a joint mission between the USA, Canada and Japan [47]. Apart from MODIS, Terra carries the Advanced Space borne Thermal Emission and Reflection Radiometer (ASTER), Clouds and the Earth's Radiant Energy System (CERES), Multi-angle Imaging SpectroRadiometer (MISR) and Measurements of Pollution in the Troposphere (MOPITT) sensors. Aqua, also commonly referred to as EOS-PM-1, was launched from the Vandenberg Air Force Base on May 4, 2002. Apart from the MODIS instrument, Aqua carries the Advanced Microwave Scanning Radiometer-EOS (AMSR-E), Advanced Microwave Sounding Unit (AMSU-A), Atmospheric Infrared Sounder (AIRS), Humidity Sounder for Brazil (HSB) and Clouds and the Earth's Radiant Energy System (CERES) sensors.

The MODIS design team put particular emphasis on instrument calibration as this is critical in generating accurate long-term time-series data for global change studies [48]. The Terra and Aqua satellites orbit the globe in a sun-synchronous orbit at an altitude of 705 km. The MODIS sensor has 36 spectral bands between 0.405 and 14.385 μm with on-board calibration systems [48]. The first two bands have a spatial resolution of 250 m with bands three to seven having a spatial resolution of 500 m. Bands eight through 36 have a spatial resolution of 1 km. The MODIS instrument makes use of a cross-track scan mirror, collecting optics and individual detector elements [49]. The swath dimensions of MODIS are 2330 km (across track) by 10 km (along track at nadir) which, at a resolution of 500 m, produces 20 lines in a single scan [49]. It should be noted however that the 500 m resolution is at nadir and that the pixels size increases slightly in the scan direction which causes pixels to be partially overlapping at off-nadir angles [50]. This is commonly known as the bow-tie effect and is a source of variability over the revisit cycle.

The MODIS instrument data are converted systematically into terrestrial, atmospheric and oceanic products. The first seven bands are typically used for land applications and are often referred to as the MODIS land bands. The bands were chosen to minimize the impact of absorption by atmospheric gases and in particular water vapor, which has been a limitation of the previous instruments for land remote sensing [41] (see section 2.2.1). Table 2.4 gives a description of the specific wavelength and

bandwidth of each of the land bands [51].

TABLE 2.4: MODIS spectral band properties and characteristics.

Band	Wavelength [nm]	Resolution [m]	Primary Use	Spectral range
Band 1	620–670	250	Land/Cloud/Aerosols Boundaries	Visible (Red)
Band 2	841–876	250	Land/Cloud/Aerosols Boundaries	Near IR
Band 3	459–479	500	Land/Cloud/Aerosols Properties	Visible (Blue)
Band 4	545–565	500	Land/Cloud/Aerosols Properties	Visible (Green)
Band 5	1230–1250	500	Land/Cloud/Aerosols Properties	Short Wave IR
Band 6	1628–1652	500	Land/Cloud/Aerosols Properties	Short Wave IR
Band 7	2105–2155	500	Land/Cloud/Aerosols Properties	Short Wave IR
Band 8	405–420	1000	Ocean Color/Phytoplankton/Biogeochemistry	Visible (Blue)
Band 9	438–448	1000	Ocean Color/Phytoplankton/Biogeochemistry	Visible (Blue)
Band 10	483–493	1000	Ocean Color/Phytoplankton/Biogeochemistry	Visible (Blue)
Band 11	526–536	1000	Ocean Color/Phytoplankton/Biogeochemistry	Visible (Green)
Band 12	546–556	1000	Ocean Color/Phytoplankton/Biogeochemistry	Visible (Green)
Band 13	662–672	1000	Ocean Color/Phytoplankton/Biogeochemistry	Visible (Red)
Band 14	673–683	1000	Ocean Color/Phytoplankton/Biogeochemistry	Visible (Red)
Band 15	743–753	1000	Ocean Color/Phytoplankton/Biogeochemistry	Near IR
Band 16	862–877	1000	Ocean Color/Phytoplankton/Biogeochemistry	Near IR
Band 17	890–920	1000	Atmospheric Water Vapor	Near IR
Band 18	931–941	1000	Atmospheric Water Vapor	Near IR
Band 19	915–965	1000	Atmospheric Water Vapor	Near IR
Band 20	3660–3840	1000	Surface/Cloud Temperature	Mid Wave IR
Band 21	3929–3989	1000	Surface/Cloud Temperature	Mid Wave IR
Band 22	3929–3989	1000	Surface/Cloud Temperature	Mid Wave IR
Band 23	4020–4080	1000	Surface/Cloud Temperature	Mid Wave IR
Band 24	4433–4498	1000	Atmospheric Temperature	Mid Wave IR
Band 25	4482–4549	1000	Atmospheric Temperature	Mid Wave IR
Band 26	1360–1390	1000	Cirrus Clouds Water Vapor	Near IR
Band 27	6535–6895	1000	Cirrus Clouds Water Vapor	Mid Wave IR
Band 28	7175–7475	1000	Cirrus Clouds Water Vapor	Long Wave IR
Band 29	8400–8700	1000	Cloud Properties	Long Wave IR
Band 30	9580–9880	1000	Ozone	Long Wave IR
Band 31	10780–11280	1000	Surface/Cloud Temperature	Long Wave IR
Band 32	11770–12270	1000	Surface/Cloud Temperature	Long Wave IR
Band 33	13185–13485	1000	Cloud Top	Long Wave IR
Band 34	13485–13785	1000	Cloud Top	Long Wave IR
Band 35	13785–14085	1000	Cloud Top	Long Wave IR
Band 36	14085–14385	1000	Cloud Top	Long Wave IR

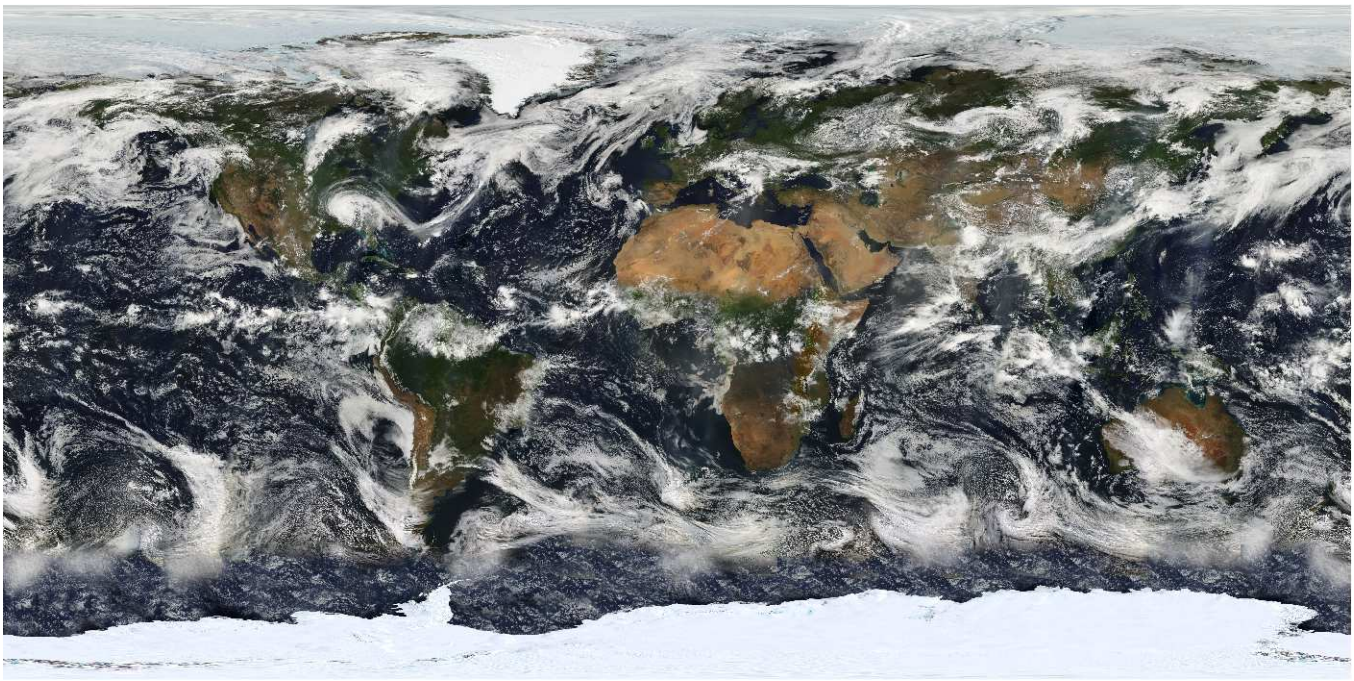

FIGURE 2.15: MODIS mosaic of the Earth [52].

TABLE 2.5: MODIS land products.

Code	Platform	Description
Radiation balance product suite		
MOD09 / MYD09	Aqua / Terra	Surface Reflectance
MOD11 / MYD11	Aqua / Terra	Surface Temperature and Emissivity
MOD43 / MYD43 / MCD43	Aqua / Terra / Combined	BRDF/Albedo
MOD43 / MYD43 / MCD43	Aqua / Terra / Combined	BRDF/Albedo
Vegetation Product Suite		
MOD13 / MYD13	Aqua / Terra	Vegetation Indices
MOD15 / MYD15 / MCD15	Aqua / Terra / Combined	Leaf Area Index - FPAR
MOD17 / MYD17	Aqua / Terra	Gross Primary Productivity
Land-Cover Product Suite		
MOD12 / MCD12	Aqua / Combined	Land-Cover Type
MOD14 / MYD14	Aqua / Terra	Thermal Anomalies and Fire
MOD44	Aqua	Vegetation Continuous Fields

Because of the large swath size, the same location can be observed every one to two days. It should be noted that that the viewing angle of these daily observations differ from one another in a repeating

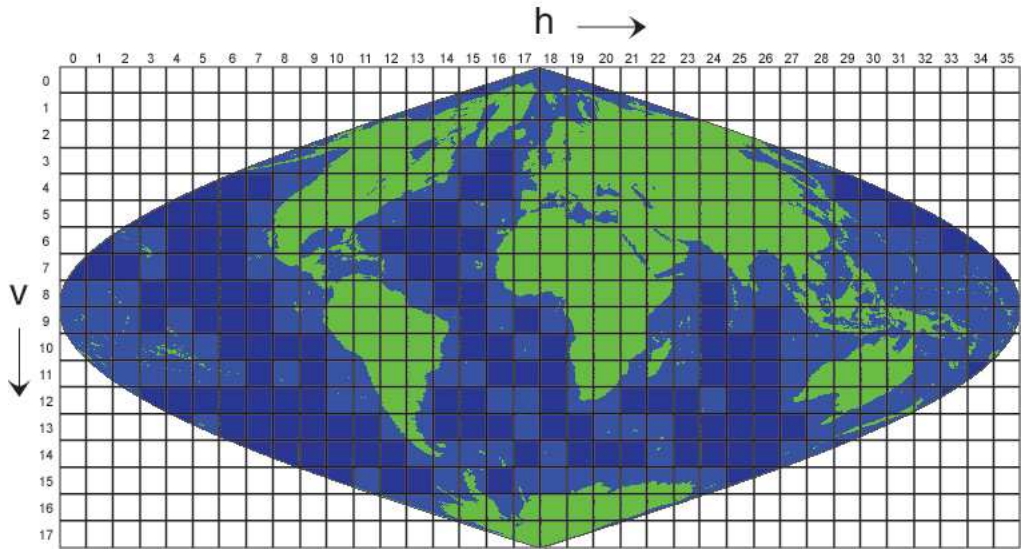

FIGURE 2.16: MODIS sinusoidal projection [27].

pattern of 16 days. The reason for this is that the MODIS instrument repeat cycle of nadir overpasses is 16 days which implies that every 16 days the MODIS instrument will be traveling on nearly the exact same path [49]. The radiometric resolution of the sensor is 12 bits, which results in 4096 unique levels (2^{12}). A color composite image using the MODIS instrument is shown in Figure 2.15. Table 2.5 shows some of the most common MODIS products.

The data product that was chosen in this thesis was MCD43A4 For a complete list of MODIS products see [27]., which is based on the MCD43 BRDF/Albedo radiance product (Table 2.5). The prefix "MOD" and "MYD" of the product code refers to data acquired using the Aqua and Terra satellites respectively. The "MCD" prefix is used to indicate that data from both satellites were used. The MCD43A4 product is derived using a surface reflectance product which is defined as being the measured reflectance from the land surface in the absence of the atmosphere and performs corrections for the effect of gaseous absorption, molecules and aerosol scattering [33, 51]. The MCD43A4 product also takes into account the BRDF (See section 2.2.2) to adjust the reflectance values as if they were taken from nadir view. It does this by utilizing 16 days' worth of multi-date data of both the Terra and Aqua satellites together with a semi-empirical kernel-driven bidirectional reflectance model to determine a global set of parameters describing the BRDF of the land surface. This is then used to determine the hemispherical reflectance as well as the bi-hemispherical reflectance at the solar zenith angle corresponding to local solar noon to produce a coarse resolution (500 m for all bands) composite image every 8 days [28].

TABLE 2.6: Coefficients for equations 2.5 and 2.6.

Term	Isotropic (iso)	RossThick (vol)	LiSparseR (geo)
g0	1.0	-0.007574	-1.284909
g1	0.0	-0.070987	-0.166314
g2	0.0	0.307588	0.041840
g	1.0	0.189184	-1.377622

The algorithm used for BRDF correction uses a kernel-driven, linear BRDF model having a weighted sum of an isotropic parameter and two functions of viewing and illumination geometry used to determine reflectance [28]

$$R(\theta, v, \phi, \lambda) = f_{\text{iso}}(\lambda) + f_{\text{vol}}(\lambda)K_{\text{vol}}(\theta, v, \phi, \lambda) + f_{\text{geo}}(\lambda)K_{\text{geo}}(\theta, v, \phi, \lambda), \tag{2.4}$$

where θ is the solar zenith angle, v is the view zenith, ϕ is the relative azimuth angle and λ is the wavelength. $K_{\text{vol}}(\theta, v, \phi, \lambda)$ is derived from volume scattering radiative transfer models and $K_{\text{geo}}(\theta, v, \phi, \lambda)$ is derived from geometric shadow casting theory. The RossThick kernel expression for K_{vol} and the LiSparce kernel expression for K_{geo} have been identified as the best suited combination for the operational MODIS BRDF/Albedo algorithm [28].

BRDF model parameters are provided in the MOD43B1 product and can be used to compute the albedos with the solar illumination geometry by making use of the following polynomial used to model black-sky and white sky albedos respectively

$$\begin{aligned}\alpha_{\text{bs}}(\theta, \lambda) = f_{\text{iso}}(\lambda)(g_{0\text{iso}} + g_{1\text{iso}}\lambda^2 + g_{2\text{iso}}\lambda^3) + \\ f_{\text{vol}}(\lambda)(g_{0\text{vol}} + g_{1\text{vol}}\lambda^2 + g_{2\text{vol}}\lambda^3) + \\ f_{\text{geo}}(\lambda)(g_{0\text{geo}} + g_{1\text{geo}}\lambda^2 + g_{2\text{geo}}\lambda^3),\end{aligned} \tag{2.5}$$

and

$$\alpha_{\text{ws}}(\theta, \lambda) = f_{\text{iso}}g_{\text{iso}} + f_{\text{vol}}g_{\text{vol}} + f_{\text{geo}}g_{\text{geo}}. \tag{2.6}$$

The coefficients used in equations 2.5 and 2.6 are given in table 2.5. In the MCD43A4 product, the solar zenith angle is transformed to the angle at local solar noon [49], which results in a high degree

of reflection consistency when using multiple images to construct a pixel time-series. The composite image is in the form of a sinusoidal projected tile. Figure 2.16 shows the sinusoidal projection tiles of $10^\circ \times 10^\circ$. Each tile is in the HDF-EOS file format having 2400×2400 pixels. This thesis focuses on the h20v11 tile (Figure 2.16). Figure 2.17 shows the outline of a 500 m×500 m MODIS pixel in the Gauteng province of South Africa, together with its corresponding seven-year time-series for all seven land bands spanning from 2001/01 to 2008/01.

When considering optical measures of vegetation canopy greenness, Vegetation Indices (VIs) are often considered [53]. VIs uses band combinations that provide consistent spatial and temporal comparisons for monitoring photosynthetic activities [48]. Two of the most common VIs will be discussed in the following section.

2.6 VEGETATION INDICES

The study of terrestrial vegetation in large-scale global processes is one of the primary interests in earth observation. This requires an understanding of the biophysical and structural properties as well as temporal variations of vegetation. Vegetation indices (VIs) are spectral transformations of two or more spectral bands designed to enhance the contribution of vegetation properties and allow comparison of terrestrial photosynthetic activity variations. VIs are widely used in the estimation of leaf area index, fraction of absorbed photosynthetically-active radiation, chlorophyll content, vegetation fraction, photosynthesis, transpiration and net primary production [54].

VI measurements combine the chlorophyll-absorbing visible red spectral region with the near-infrared (NIR) spectral region (which has a high reflection in the case of green vegetation) to provide a consistent and robust measure of area-averaged canopy photosynthetic capacity [55]. This simple transformation of spectral bands enables monitoring of seasonal, inter-annual, and long-term variations of vegetation parameters [53]. Two VIs, the normalized difference vegetation index (NDVI) and enhanced vegetation index (EVI), will be considered in this section.

2.6.1 Normalized difference vegetation index

Normalized Difference Vegetation Index (NDVI) is a vegetation index that has been successfully used in many studies related to vegetation [53]. NDVI is a normalized ratio of the Near IR and red bands,

$$\mathrm{NDVI} = \frac{\rho_{\mathrm{NIR}} - \rho_{\mathrm{red}}}{\rho_{\mathrm{NIR}} + \rho_{\mathrm{red}}}, \tag{2.7}$$

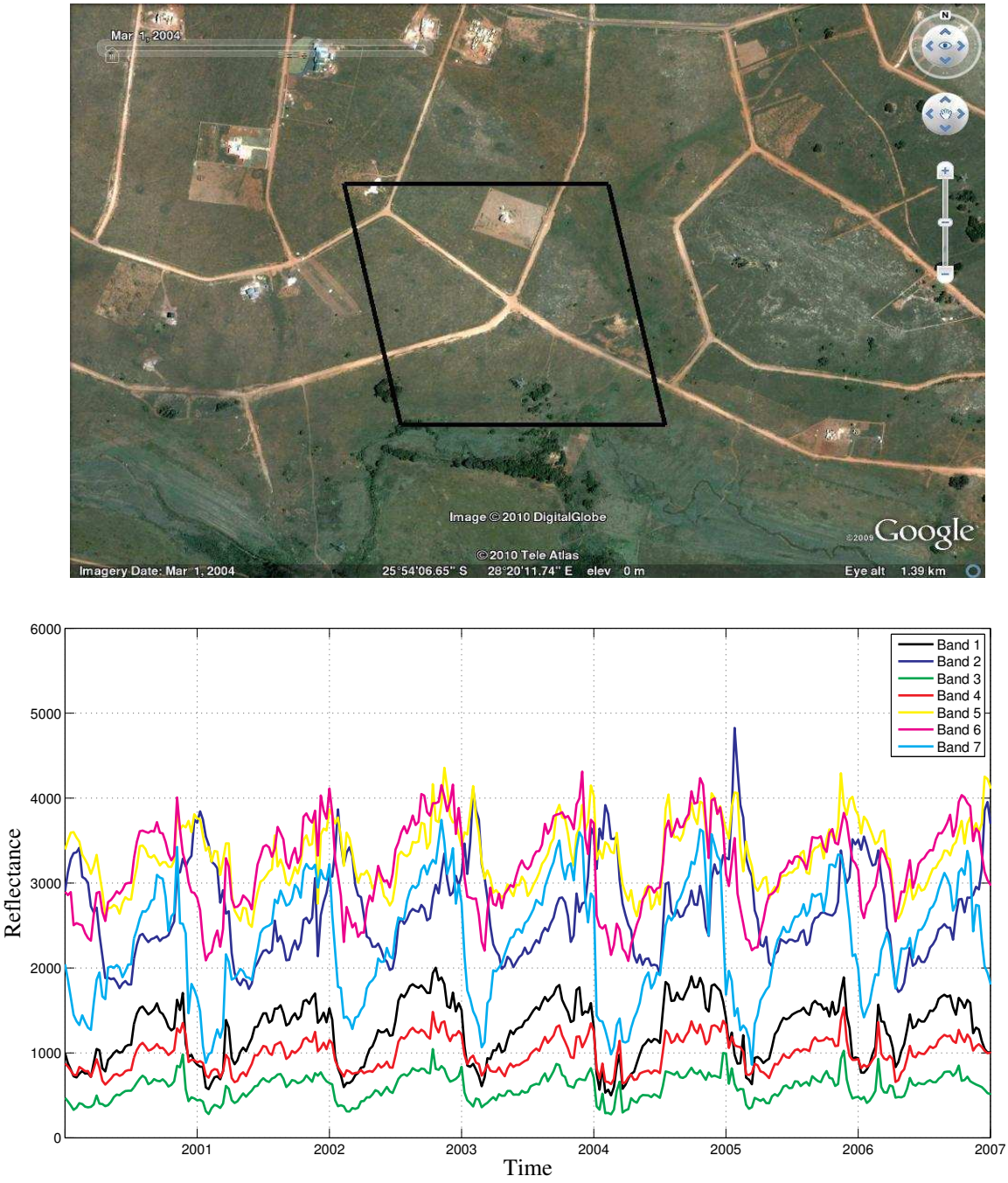

FIGURE 2.17: MODIS pixel and corresponding seven year time-series spanning from 2001/01 to 2008/01 (courtesy of Google^{TM}Earth).

where ρ_{NIR} and ρ_{red} is the surface reflectance of the Near IR and red bands respectively. These bands correspond to MODIS band two and one respectively (Table 2.4). The rationale behind the index is that Photosynthetically Active Radiation (PAR), which is in the 400–700 nm wave band, is used in the process of photosynthesis. This results in a strong absorption of these wavebands as was shown in Figure 2.9. Wavelengths longer than 700 nm are not used for photosynthesis and are reflected due to

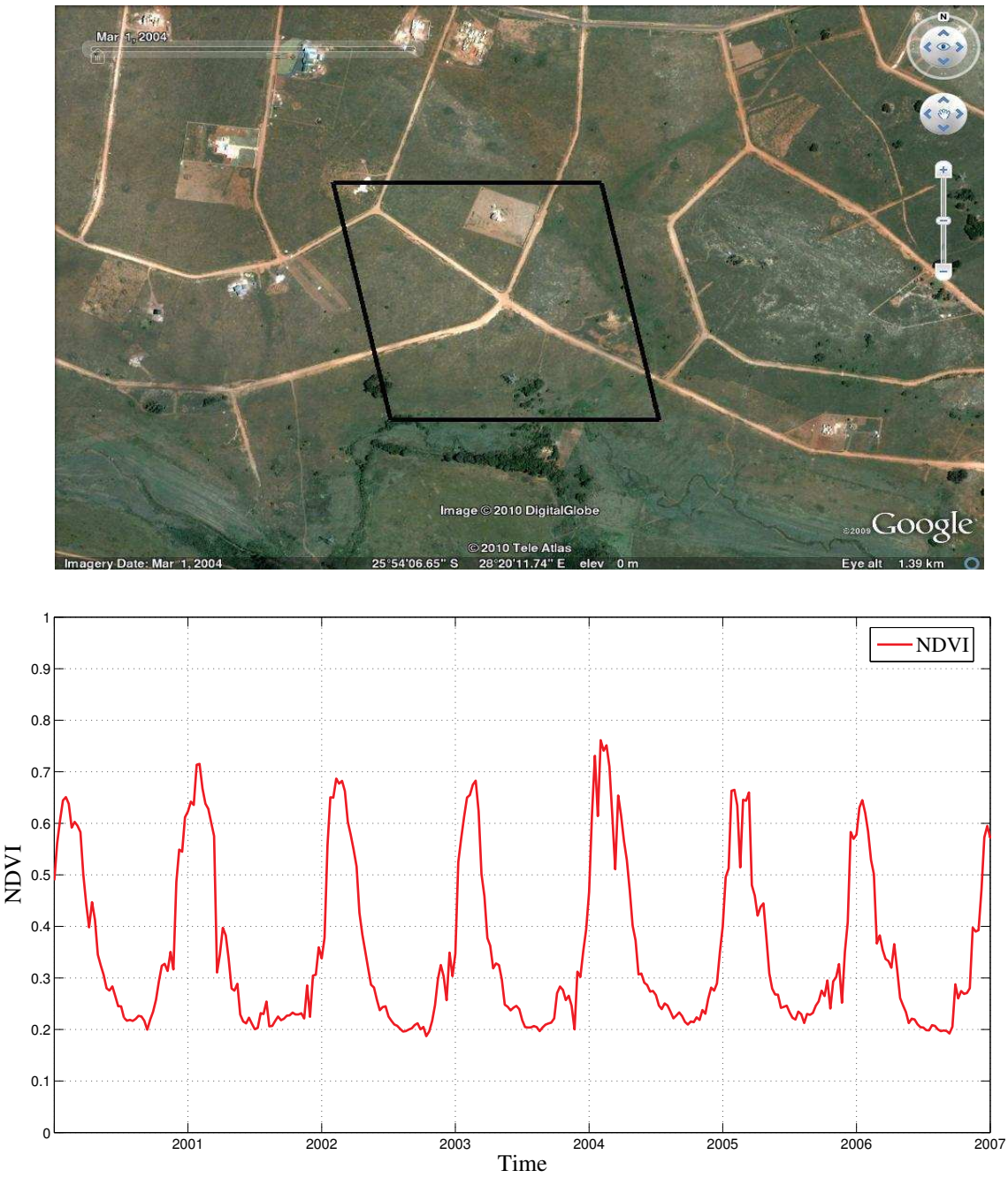

FIGURE 2.18: QuickBird image of an area in northern South Africa (courtesy of Google™Earth). A polygon representing the area covered by a 500 m MODIS pixel together with the corresponding seven-year NDVI time-series spanning from 2001/01 to 2008/01 is also shown.

the internal cell structure of green vegetation [55]. This results in the characteristic low percentage of reflection in the visible region relative to the near IR region of green vegetation (Figure 2.9).

NDVI is a good vegetation measure in the sense that its stability enables meaningful comparisons of seasonal and inter-annual changes in vegetation greenness, growth and activity [53]. NDVI time-series

data have been used in various operational applications including image segmentation methods, land-cover classification, climate studies and change detection [17, 56–58]. The NDVI time-series for the pixel shown in Figure 2.17 is shown in Figure 2.18.

2.6.2 Enhanced vegetation index

The enhanced vegetation index (EVI) optimizes the vegetation signal with improved sensitivity in high biomass regions because of an increased dynamic range, which in the case of NDVI, has a tendency to saturate in high biomass regions [53]. Vegetation monitoring is also improved through de-coupling of the canopy background signal. EVI is calculated as:

$$EVI = G\frac{\rho_{\text{NIR}} - \rho_{\text{red}}}{\rho_{\text{NIR}} + C_1 \times \rho_{\text{red}} - C_2 \times \rho_{\text{blue}} + L}, \tag{2.8}$$

where ρ_{NIR}, ρ_{red} and ρ_{blue} is the surface reflectance of the Near IR, red and blue bands respectively, L is the canopy background adjustment term, C_1, C_2 are the coefficients of the aerosol resistance term and G is the gain term. The rationale behind the the scaled blue band and red band term is based on the wavelength dependency of the aerosol effects. The blue band is more atmosphere-sensitive and is used to correct the red band for aerosol influences. The canopy background correction term (L) is used since 70% of the terrestrial surface has open canopies with canopy background signals having some effect on the canopy reflectance properties. The coefficients adopted in the MODIS EVI algorithm are, L = 1, C_1 = 6, C_2 = 7.5, and G (gain factor) = 2.5 [53].

2.6.3 Using vegetation indices for land cover change detection

NDVI is the most widely used VI when considering land cover change detection [12, 20, 57, 59–61]. This could be attributed to the simplicity of calculating the NDVI metric as well as the ability to be calculated for sensors that do not have a blue band. Our preliminary results shows that the performance of the methods presented in this study was not influenced considerably by the choice of vegetation index (NDVI vs. EVI). It was consequently decided to use NDVI time-series data as input to the change detection method presented here in order to maximize comparability with previous studies so that the change detection ability could be attributed to the method rather than the choice of index. Although only NDVI data were used, it should be noted that all the change detection methods presented in this thesis could be adapted to other vegetation indices.

2.7 CHANGE DETECTION METHODS

There is no single solution to change detection for all applications. Different change detection methods have their own merits with no single approach being optimal for all change scenarios [15]. Monitoring changes on the surface of the Earth is a dynamic topic with new techniques being continuously developed [14, 15]. There are three major steps involved when developing a change detection framework. The first step is to perform image pre-processing which includes geo-location and image registration, radiometric and atmospheric correction. The goal of this step is to ensure that the data are consistently processed through time and that changes in surface reflectance are not caused by processing artifacts. For example, if two images are not properly co-registered, the location of a pixel in the first image will not correspond with the co-located pixel in the second image, resulting in an erroneous change detection for that pixel. Various studies have shown the adverse effect on change detection accuracy in the event of mis-registration [62–64]. The second step is to implement a suitable change detection method that produces information on where and in some cases when changes occurred in the area in question. In the the third step, an accuracy assessment is performed to quantify the performance of the algorithm using a ground truth dataset.

A distinction can be made between multi-temporal and hyper-temporal change detection methods. Multi-temporal change detection methods usually takes as input a few images (in the order of 2–5) [14, 15] whereas hyper-temporal change detection methods make use of a series of images (up to hundreds) taken at regular, constant intervals, usually a few (8 – 30) days apart. The vast majority of change detection algorithms in the literature are based on medium to high resolution multi-temporal change detection with only a limited number of hyper-temporal change detection methods [14, 15].

Most multitemporal change detection methods found in the literature can broadly be classified into two categories. In the first, two pixels are used as input to a mathematical function to produce a change metric. The second step is then to classify the change metric value as having changed or not. The second category is often referred to as post-classification change detection where a labeled map is compared at two instances and corresponding areas having different labels are then flagged as change areas [14].

When considering land cover change detection, previous studies have shown that multi-temporal change detection methods that infer change based on differences in the surface reflectance at two instances tend to be performance limited due to differences in vegetation [45, 46]. Phenology-induced errors occur when a change map is generated using two images acquired at different stages of the

intra-annual growth cycle [17]. The spectral signature of the same vegetation can vary significantly through the year (Figures 2.10 and 2.11) which could lead to an elevated false alarm rate as the difference in ground reflection between the two acquisitions is not only caused by changes in land cover, but also by a natural seasonal variation in the spectral signature of vegetation. The temporal frequency of the satellite should thus be high enough to distinguish change events from natural seasonal changes in vegetation. Apart from these natural seasonal variations, changes in ecosystems can broadly be classified as being gradual (trend) or abrupt. As the name suggests, gradual change refers to a slow deviation of the time-series caused by, for example, land degradation. Abrupt change refers to an abrupt change in the time-series caused by, for example, deforestation [29]. Therefore, hyper-temporal change detection methods should be able to distinguish phenological cycles from trends or abrupt change in land cover [20, 29, 65]. Another important motivation for using hyper-temporal change detection methods is the need for automated change detection over large areas [66]. While the majority of change detection methods are focused on changes between satellite images from two dates [14, 15], the increasing availability of large archives of historical images makes it possible to develop richer algorithms that fully exploit the temporal dimension of the data. Rather than only focusing on high resolution image to image change detection, it can be complemented by hyper-temporal time-series data. In line with GEOSS philosophy [31], these datasets can be aggregated as a multi-sensor monitoring system and change information obtained using hyper-temporal data could be used to guide high-resolution sensors in acquiring imagery of areas of interest identified using the medium resolution time-series data. Another advantage of hyper-temporal time-series data is that continuous monitoring is possible as the data is not limited to the availability of costly sets of high-resolution images.

Post classification change detection is also not without its challenges. In concept, identifying areas where the class labels are different for two land cover maps is intuitive, but this process relies heavily on the classification accuracy of each of the two land cover maps. The selection of optimal image dates, for example, is crucial since differences in reflectance can be caused by seasonal vegetation fluxes and Sun angle differences which could cause a difference in the the land cover classification for areas that have similar land cover types in both images [14]. For South Africa, two major land cover mapping efforts were made to produce a land cover database in 1994 and 2000, referred to as the South African National Land-Cover (NLC) 94 and NLC 2000 datasets respectively [67]. These datasets were used to determine a change map by comparing the class labels for each pixel. Unfortunately, the 1994 and 2000 versions of the NLC were compiled using very different methods. The NLC 94 had a a minimum mapping unit of 25 ha, and contained 31 land-cover classes whereas the NLC 2000 had a

minimum mapping unit of 2 ha, and contained 45 land-cover classes [67]. Converting these classes into comparable pixel sizes and land cover classes was not a trivial task and taking into consideration that the original classification accuracy of the land cover datasets where 79.4% and 65.8% respectively, the production of a highly accurate land cover change map using this post-classification change detection approach proved challenging [67].

Some of the typical methods used in classical multitemporal change detection, for example image differencing [68–71] , image regression [72], image rationing, vegetation index differencing [73], Principle Component Analysis (PCA) [59, 61] and Change Vector Analysis (CVA) [74], can be adapted to the hyper-temporal case by considering a multitemporal subset of the time-series. For example, in CVA a change vector can be described by an angle of change and a magnitude of change between the reflectance values of multiple bands between two dates. This concept was extended to the hyper-temporal case in [74] by constructing a vector containing a series of biophysical parameter observations within a single year and comparing this vector with the corresponding vector for the following year. The consequent change vector is then analyzed to infer a change or no-change decision. For example, if an NDVI time-series sampled every month is available, a vector containing 12 NDVI values (representing one year) are compared with the corresponding vector for the following year. The idea is that the magnitude and angle of the consequent change vector gives an indication of the change occurring over these consecutive years. The potential problem with this approach, however, is that the change detection is essentially a comparison across multiple instances, comparing two at a time, and does not fully utilize the temporal dimension of the signal.

2.7.1 Hyper-temporal time-series analysis

Time-series analysis comprises of methods that attempt to understand the underlying force structuring the data, identifying patterns and trends, detecting changes, clustering, modeling and forecasting [75]. Because of the high revisit frequency that is required in constructing a hyper-temporal time-series, the data from coarse and medium resolution wide-swath sensors is primarily applicable (section 2.4). In the following section, emphasis will be placed on methods that can be classified as hyper-temporal change detection methods. These methods can be broadly classified into 3 classes namely, regression analysis, Fourier analysis and temporal metrics.

2.7.1.1 Regression Analysis

A fairly common method for change detection using hyper-temporal data is regression analysis. Here, a basic assumption of the underlying form of the data is made, for example a linear trend, and

the parameters of the assumed function is estimated using the observed data. R.E. Kennedy *et al.* considered a set of hypothesized temporal trajectories associated with forest disturbance dynamics [66]. If the time-series fits the idealized trajectory according to a least-squares measure of goodness of fit, it is inferred that the time-series in question experienced the phenomenon described by that trajectory. A similar approach for estimating proportional forest cover change was proposed by D.J. Hayes *et al.* by making use of a regression model and subsequent comparison to reference change data sets derived from Landsat data for a study site in Central America [76]. The advantage of these type of methods is that there is no threshold requirement as a direct classification is made based on the best fit in a finite set of hypothesized temporal trajectories. The disadvantage however is that the performance of methods based on regression analysis depends on the assumption that is made on the form of the hypothesized temporal trajectories. For example, if it is assumed that the temporal trajectory of a hypothesized disturbance will follow the form of a downward step function (i.e. instantaneous drop in reflectance) and the actual temporal trajectory is better described by an exponential decay function, the disturbance in question would not be well represented by the idealized step function. It follows that if the temporal trajectory in question is not well represented by any of the hypothesized trajectories, the change detection method will not perform well. For the method to work in a more general context, a very large dataset of hypothesized trajectories associated with change events will be required as all types of possible changes would have to be characterized, making the approach somewhat impractical for monitoring large heterogeneous areas.

2.7.1.2 Fourier Analysis

Another approach often used when considering hyper-temporal time-series data is Fourier analysis. Fourier analysis expresses a time-series as the sum of a series of cosine waves with varying frequency, amplitude and phase [77]. The frequency of each cosine component is related to the number of completed cycles over the defined interval. The Fast Fourier Transform (FFT) is an effective and computationally efficient algorithm to compute the Discrete Fourier Transform (DFT) [77] and is often used when evaluating satellite time-series data [56–58, 78]. In many applications where the FFT transformation of time-series data is used for classification and segmentation, only the first few FFT components are considered as they tend to dominate the spectrum [56–58]. The reason for this is because of the strong seasonal component and slow variation relative to the sampling interval of the time-series. It has been found that even when considering only the mean and seasonal FFT components [56], reliable class separation can be achieved. A drawback of using FFT-based methods is that the underlying process is assumed to be stationary. This assumption is often invalid in the case of NDVI time-series data, especially if a land cover change is present. Although this method is mostly

used for classification, there has been some recent research interest to use the FFT to perform change detection. For example, B.P. Salmon *et al.* proposed that a sliding window FFT method be used to perform change detection [79]. J. Verbeselt *et.al.* used Fourier analysis as a major step in modeling the seasonal component used in the BFAST (Breaks For Additive Seasonal and Trend) approach [29]. The model used 3 harmonic terms and was found to be more suitable and robust for phenological change detection than the piecewise linear seasonal model using seasonal dummy variables that was employed by the same author in [65].

2.7.1.3 Temporal Metrics

Most of the change detection methods using coarse or medium resolution hyper-temporal time-series are used to detect climate-driven change, phenological modifications and net-primary production on a large scale [16, 17, 19, 80]. J. Borak used temporal change metrics as a land-cover change detection method [16]. These metrics were computed by considering the inter-annual difference of five temporal metrics (annual maximum, annual minimum, annual range, annual mean and temporal vector) as well as two spatial metrics (spatial mean and spatial standard deviation), i.e. year2 $-$ year1, for all combinations of the aforementioned spatial and temporal metrics [16]. The underlying idea is that these metrics are compared to a threshold value to determine whether a change or no-change decision should be made. C. Potter used the moving average of the time-series to label pixels as as having changed when the time-series deviated significantly (greater than 1.7 standard deviations) from the 18-year average of the time-series for at least 12 consecutive time-steps [81].

D.J. Mildrexler and N.C Coops used a disturbance index (DI) to detect large-scale ecosystem disturbances [18, 19]. The disturbance index is calculated as:

$$DI_{\mathrm{LST/EVI}} = \frac{LST_{\mathrm{max}}/EVI_{\mathrm{max}}}{LST_{\overline{\mathrm{X}}\mathrm{max}}/EVI_{\overline{\mathrm{X}}\mathrm{max}}}, \tag{2.9}$$

where $DI_{\mathrm{LST/EVI}}$ is the disturbance index, LST_{max} is the annual maximum land surface temperature, EVI_{max} is the annual maximum Enhanced Vegetation Index (EVI), $LST_{\overline{\mathrm{X}}\mathrm{max}}$ is the multi-year mean of LST_{max} and $EVI_{\overline{\mathrm{X}}\mathrm{max}}$ is the multi-year mean of EVI_{max}. From (2.9) it is clear that the disturbance index is calculated on an annual basis. The DI can then be compared to a pre-defined threshold to infer a change or no-change decision.

R.S Lunetta derived a change metric by computing the difference in total annual NDVI for a range of pixels in the given study area and isolating the pixels having an abnormal (relative to the other pixels in the study area) reduction in annual NDVI [17]. The threshold is selected by using standard normal

statistical analysis.

The methods described in [16–18,81] all work on the principle that when a pixel departs from a normal temporal profile, a change event is detected by comparing the change metric to a threshold value. The change metric that is calculated by the majority of hyper-temporal change detection methods mostly uses an annual composite of the hyper-temporal time-series, for example, the annual NDVI maximum [16], annual maximum land surface temperature [18] or total annual NDVI [17]. Thus, when only the total annual NDVI of a seven-year time-series (sampled every eight days) is used when calculating a change metric, the original time-series, which contains more than 300 samples, is effectively reduced to only 7 samples which decreases the information content of the original time-series considerably. The second consideration is the selection of suitable thresholds. In most of the current hyper-temporal change detection methods in the literature, *a-priori* knowledge of the probability of land-cover change is required when selecting a suitable threshold and more often than not a trial-and-error approach is used in determining these thresholds. In this thesis it is proposed that simulated land cover change be used to determine a suitable threshold. The change metric is calculated for each pixel in a no-change and simulated change dataset and the threshold that best separates the aforementioned datasets is then used. The operator thus only needs to provide examples of no-change time-series, which, unlike change examples is very easy to obtain.

2.7.2 MODIS land cover change products

Although some MODIS change detection products do exist (such as MODIS burn-scar detection [82]), there are currently no operational MODIS products available specifically for land cover change detection. There were however two previous attempts to implement an automated MODIS land cover change product, as an operational system. The first was the MODIS Vegetative Cover Conversion (VCC) product, which uses MODIS 250 m surface reflectance data, and was designed to serve as a global alarm for land cover change caused by anthropogenic activities and extreme natural events [12]. The product was to serve as an alarm which could be augmented by higher resolution sensors such as Landsat 7, Ikonos, and QuickBird once detected. Five change detection methods where proposed [12]:

1. The Red-NIR space partitioning method : Uses a two-dimensional representation of the brightness (mean of band one and two) and greenness (difference between band two and one) at different times to identify change pixels.

2. Red-NIR space change vector: By considering a pixels location in the Red-NIR space at two different dates, the starting and ending positions, direction, and magnitude of the change vector

are used to identify a change event.

3. Modified delta space thresholding: Uses a space defined by differences in pixel values for times 1 and 2 for the red and NIR values of each pixel (no change occurs at the origin). Type of conversion is defined by the angle and distance from the origin and the initial state of the pixel.

4. Texture: Uses the coefficient of variation of the NDVI within a 3×3 kernel at times 1 and 2. When the coefficient of variation exceeds a pre-defined threshold value, a change is flagged.

5. Linear feature: Compute the mean of the absolute difference of the pixel value for each neighboring pixel in a 3×3 kernel. A threshold determines whether a linear feature is present.

The second MODIS land cover change detection product that was proposed was the MODIS Land Cover and Land-Cover Change Algorithm Theoretical Basis Document (ATBD) [83]. The ATBD suggested that the primary change detection technique for the 1 km Land-Cover Change Parameter is change vector analysis [84]. In this technique, a change vector is used to connect two points in multitemporal space. These two points represents an annual multitemporal set of indicator values. The underlying idea is that the change vector is compared to a threshold value, and, when exceeded, a change decision is made. The ATBD also suggested that neural network classifiers be used on a pixel-by-pixel basis to track the probability that a specific pixel changes classes over time. The artificial neural network is used in a supervised manner to develop the Land Cover Parameter. New data that are presented to the neural network is either classified as matching an existing category, or a new category must be created. By monitoring the classification on a per-pixel basis, change can be detected.

When considering the proposed VCC product [12], as well as the change vector analysis method described in the ATBD [84], none of these methods fully utilize the temporal dimension as only two instances are compared rather than considering the complete temporal profile (As discussed in section 2.7.1) and effectively disregards a large suite of time-series methods used in other disciplines e.g. signal processing, telecommunications, etc. The neural network method proposed in the ATBD does show promising results but it should be noted that if a new data presentation does not match an existing category, then it will be necessary to determine whether the new data represent a fundamentally new condition or whether the vigilance parameter needs to be relaxed so that an existing category can now accommodate the new input. This implies that the approach is very sensitive to selection of the vigilance parameter, making the practicality of this approach questionable.

Regardless of the concerns with the proposed MODIS change detection methods, none of these proposed methods were implemented operationally, despite the fact that land cover change detection

was one of the primary objectives of the MODIS sensor [48]. Automated land cover change detection using MODIS data is therefore an ongoing endeavor.

2.8 SUMMARY

In this chapter, the basic principles of electromagnetic radiation were shown together with a description of the properties of the electromagnetic source, which, in the case of optical remote sensing, is the Sun. The interaction of electromagnetic radiation with the atmosphere and land surface was discussed. A brief comparison of sensors showed that there is a trade-off between spatial and temporal resolution. In general, medium-resolution sensors have a much wider swath width compared to high resolution sensors. This implies that when considering a global systematic acquisition strategy, a high resolution image of the same area will be available every couple of months as opposed to the near-daily acquisition of wide swath sensors. This point is crucial as the same area can differ in appearance at different stages of the natural growth seasonal cycle [17]. For this reason, the high temporal frequency provided by medium resolution sensors was opted for. The MODIS sensor was chosen for this thesis, a list of available MODIS products as well the band specifications were given. The MCD43A4 BRDF corrected product was chosen because of the high degree of consistency between images which, in turn, provided accurate surface reflectance time-series information despite large variations in viewing angles. Most change detection methods use multi-temporal data as input and numerous solutions to this class of problem have been presented in the literature. The use of hyper-temporal time-series data for change detection is not as well documented in the literature and most methods that make use of hyper-temporal time-series data for change detection focused on large scale phenological and climate driven changes instead of anthropogenic land cover changes. A novel change detection formulation is thus required when considering change detection for smaller areas that are typically affected by human activities such as new informal settlement developments.